

Key Points:

- Feedbacks between subglacial water flow and ice melt determine the rate of incision of drainage channels, depending on their spacing
- We derive a threshold meltwater input above which channels form under glaciers, a function of ice thickness and geothermal flux
- Including lateral heat transport allows continuum models of subglacial hydrology to reproduce Röthlisberger channel behavior

Supporting Information:

Supporting Information may be found in the online version of this article.

Correspondence to:

K. L. P. Warburton,
klpw3@cam.ac.uk

Citation:

Warburton, K. L. P., Meyer, C. R., & Sommers, A. N. (2024). Predicting the onset of subglacial drainage channels. *Journal of Geophysical Research: Earth Surface*, 129, e2024JF007758. <https://doi.org/10.1029/2024JF007758>

Received 28 MAR 2024
Accepted 2 DEC 2024

Author Contributions:

Conceptualization: K. L. P. Warburton, C. R. Meyer

Formal analysis: K. L. P. Warburton

Investigation: K. L. P. Warburton, C. R. Meyer

Methodology: K. L. P. Warburton

Software: K. L. P. Warburton, A. N. Sommers

Supervision: C. R. Meyer

Visualization: K. L. P. Warburton, A. N. Sommers

Writing – original draft:

K. L. P. Warburton

Writing – review & editing: C. R. Meyer, A. N. Sommers

Abstract The sliding speed of glaciers depends strongly on the water pressure at the ice-sediment interface, which is controlled by the efficiency of water transport through a subglacial hydrological system. The least efficient component of the system consists of “distributed” flow everywhere beneath the ice, whereas the “channelized” drainage through large, thermally eroded conduits is more efficient. To understand the conditions under which the subglacial network channelizes, we perform a linear stability analysis of distributed flow, considering competition between thermal erosion and viscous ice collapse. The calculated growth rate gives a stability criterion, describing the minimum subglacial meltwater flux needed for channels to form, but also indicates the tendency to generate infinitely narrow channels in existing models. We demonstrate the need to include lateral heat diffusion when modeling melt incision to resolve channel widths, which allows continuum models to recover Röthlisberger channel behavior. We also show that low numerical resolution can suppress channel formation and lead to overestimates of water pressure. Our derived channelization criterion can be used to predict the character of subglacial hydrological systems without recourse to numerical simulations, with practical implications for understanding changes in ice velocity due to changes in surface melt runoff.

Plain Language Summary Glacier sliding speed depends on the degree of lubrication by water at the bed. During summer months, when there is a lot of water present, heat produced by the water flow can melt large channels into the base of the ice. These channels efficiently drain water out from the bed of the glacier, slowing down the ice flow. We study when and where channels are likely to form by considering whether local increases in water depth grow larger via positive feedback loops, or shrink away. We also look at ways to make simulations less prone to numerical artifacts. We develop a criterion for when channels form and show that our criterion matches the results of numerical simulations, but is much faster to calculate. This can be used to efficiently predict meltwater drainage beneath glaciers, seasonal patterns of ice velocity, and how these will evolve under warming conditions.

1. Introduction

The Greenland Ice Sheet is a major contributor to sea-level rise due to widespread thinning and melting of the ice (Mouginot et al., 2019; Otosaka et al., 2023). Greenland’s glaciers transport ice from the interior of the ice sheet to the ablation zone around the margin. The speed of ice flow is in large part due to sliding at the bed (MacGregor et al., 2016; Maier et al., 2019; Rignot & Mouginot, 2012), the rate of which depends strongly on the effective pressure, defined as the difference between the pressure exerted by the overlying ice and the water pressure (e.g., Helanow et al., 2021; Schoof, 2005, 2023; Warburton et al., 2023). Thus, understanding the future of the Greenland Ice Sheet requires an understanding of the way subglacial water pressure evolves in time, over a melt-season and over several decades (Aschwanden et al., 2019; Nienow et al., 2017).

Subglacial hydrological networks span a continuum from inefficient, distributed flow through connected cavities and sediment layers, to channelized, efficient drainage pathways (Schoof, 2010). The transition between distributed and channelized drainage is thought to play a large role in the seasonal patterns of ice sheet velocity across Greenland (Bartholomew et al., 2011; I. J. Hewitt, 2013) and during glacier surges (Benn et al., 2019). For a given volume of surface meltwater passing through the subglacial environment, distributed systems will show higher inland water pressure, lower effective pressure, lower basal friction, and faster flow speeds as compared to the channelized network. Throughout a melt season, basal water pressure generally increases, leading to faster glacier flow (Zwally et al., 2002), until in some cases channelization initiates, the bed drains, and the ice slows (I. J. Hewitt, 2013).

© 2024. The Author(s).

This is an open access article under the terms of the [Creative Commons Attribution License](https://creativecommons.org/licenses/by/4.0/), which permits use, distribution and reproduction in any medium, provided the original work is properly cited.

Depending on whether the summertime velocities are above or below the winter average, Greenland outlet glaciers can be categorized by type (Moon et al., 2014; Poinar, 2023; Vijay et al., 2021). This categorization shows some spatial clustering of seasonal patterns, but also reveals that the response of a single glacier can change year-on-year based on the climatic conditions, and neighboring glaciers can respond quite differently (Tedstone et al., 2015). Models of summertime hydrology often assume that no channels persist through the winter, but some studies show persistent winter channels (Hager et al., 2022; Sommers et al., 2023). Thus a small velocity response could be attributable either to no channelization during the summer or persistent channelization during the winter. Understanding the drivers of current seasonal velocity trends, by predicting when glaciers have channelized subglacial networks, would give better constraints on their future evolution in a changing climate. Models of future ice sheet evolution generally rely on current estimates of basal slipperiness, which is strongly affected by basal effective pressure and therefore by subglacial channelization (e.g., Morlighem et al., 2010; Seroussi et al., 2013; Shapero et al., 2016).

Direct observations of subglacial channels, particularly of their spatial patterning and evolution over a melt-season, are limited (e.g., Andrews et al., 2014; Rada & Schoof, 2018). The question of which glaciers have subglacial channels is therefore often left purely to numerical models of the hydrology. However, given the number of such models (c.f. Flowers, 2015), and the differing choices in their modeled processes and parameterizations (e.g., Brinkerhoff et al., 2021), the question persists: what balances govern the instability of distributed water flow and its tendency to channelize, to what extent are these model-dependent (c.f. de Fleurian et al., 2018), resolution dependent, versus robust physical properties expected of the flow.

Walder (1982), in an early study of subglacial water flow, noted the tendency of sheet (distributed) flow to go unstable in ways that rapidly become unphysical, with thicker regions of the sheet able to generate more dissipative heating and melt into the ice above. Beyond this linear instability, nonlinear features such as channels must form (Schoof, 2010). To study this in numerical simulations, many models (c.f. Flowers, 2015; Werder et al., 2013) employ separate equations for the distributed and channelized flow, turning off dissipative heating in the distributed regions to prevent this instability from occurring in domains that are designated as sheet flow.

In the Subglacial Hydrology And Kinetic, Transient Interactions model (SHAKTI; Sommers et al. (2018)), a single laminar-to-turbulent transitional water-flow model is imposed throughout the domain, and all components of the melt-rate are included everywhere. This allows channel-like features to appear at self-determined locations anywhere in the domain. However, despite the ability of the model to produce channel-like features, these features are always one grid point wide, indicating a collapse to the smallest scales, limited only by resolution of the simulation. Further, the spacing, inland extent, and in some cases the appearance of channels itself all depend on the grid size chosen, similar to features noted in models of marine ice sheets (Cornford et al., 2016).

This tendency toward an infinite narrowing of unstable features, referred to in the context of classical stability analysis as an “ultraviolet catastrophe,” is, as described by I. J. Hewitt (2011), indicative of an ill-posed mathematical model for the system, in which the shortest wavelengths are the most unstable, a sign that a process neglected in the model should become important. In his thesis, I. J. Hewitt (2009) derived a maximum growth rate for distributed flow and provided a physical argument that such a breakdown ought to occur given the model components. The particular case with no downstream variation was shown mathematically to break down by Schoof et al. (2012). We also see the ultraviolet catastrophe in the non-convergence of the SHAKTI equations when implemented in adaptive mesh schemes (Felden et al., 2023), in which the channels continue to narrow toward infinitely small scales. In contrast, a well-posed model should display wavelength selection, where a perturbation with intermediate wavelength produces the highest growth rate. Felden et al. (2023) regularized their SUBglacial Hydrology MOdel (SUHMO), by introducing a numerically motivated diffusion-like term and found this produced convergent channel widths.

In this paper, we re-investigate the instability of channel initiation, find the means to represent channels in a satisfying way within a continuum model, and derive a criterion for rapidly calculating whether or not a drainage system will channelize. We begin by completing the linear stability analysis of distributed flow, reviewing the stability criterion of I. J. Hewitt (2009), and confirming the existence of the short-wavelength blow-up. We also use this to explore the stability of long-wavelength features, and show how this could lead low-resolution simulations to numerically suppress channel formation. We then revisit the origin of the melt-rate equation and locate a missing diffusion-like term, which is similar though not identical to the form posited in Felden et al. (2023). We find that this term, which we show comes from lateral diffusion of heat, regularizes the stability analysis and

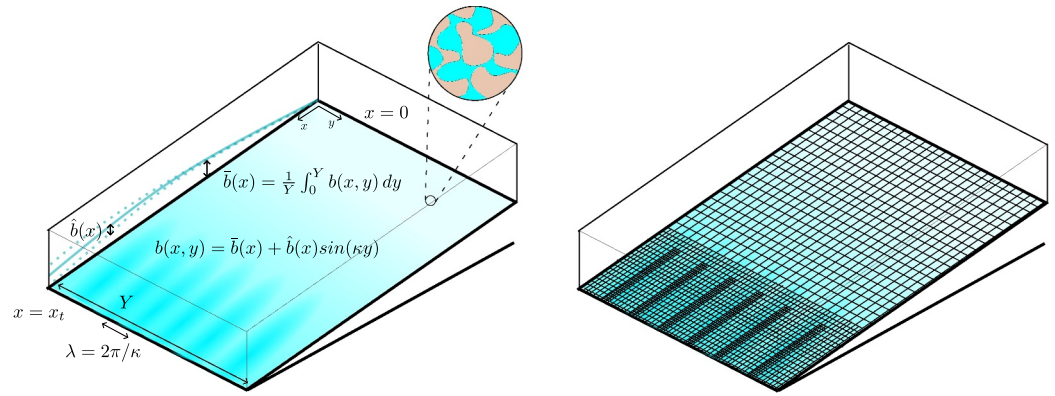


Figure 1. Left, the geometry used in this paper, showing the ice divide at $x = 0$, the terminus as x_t , and an example gap height distribution $b(x, y)$ (color), with width-average $\bar{b}(x)$ and variation of size $\hat{b}(x)$ at a wavelength λ . The spatial structure of pressure head and flux is similarly decomposed into an average plus a periodic perturbation. Away from channels, the effective gap height b represents a local average over flow through connected cavities (inset). Right, a schematic showing mesh refinement in the numerical simulations, with finer meshes in areas of higher spatial variability. Each step in refinement halves the grid size. Both the minimum and maximum levels of refinement can be set manually and we use up to 10 levels (compared to the 3 shown here). Only perturbations where λ is at least twice the minimum grid size can be resolved numerically.

allows for wavelength selection, indicating that we have found a well-posed model of the system. In the final section of the paper, we implement our new set of equations in an adaptive mesh scheme, and demonstrate that our linear stability analysis predicts the model results without need for simulation. We show that channel onset is predicted by our stability criterion, and end by discussing the applicability of this work to predicting seasonal trends in subglacial hydrology.

2. Analysis of Existing Models for Distributed Subglacial Flow

2.1. Model Governing Equations

In this work, we take as our governing equations those of SHAKTI (Sommers et al., 2018), but, by design, our results are largely independent of the exact formulation. The main difference between SHAKTI and other models of subglacial flow is the form of the power-law relating the flux, water depth, and pressure gradients (see Section 3.2). That choice can be changed in the following analysis with only a quantitative, not qualitative difference to the results.

We consider a water-filled space between the ice and bed with effective gap-height b (Figure 1), through which flows a flux of meltwater \mathbf{q} . If the rate at which melt erodes the water-ice interface over a given area is \dot{m} , then conservation of mass in the fluid layer, balancing changes in gap height with lateral flow of meltwater and local water sources, is given by

$$\frac{\partial b}{\partial t} + \nabla \cdot \mathbf{q} = \frac{\dot{m}}{\rho_w} + i_{eb}, \quad (1)$$

where ρ_w is the density of water (so \dot{m}/ρ_w is the volume of water produced by basal melt, per unit area and time) and i_{eb} is the rate at which surface meltwater is delivered to the bed. All variables used in the paper are defined in Table 1.

Tracking the vertical motion of the ice-water interface due to melting upwards, the downwards viscous collapse of the overlying ice, and opening by sliding over bumps, we have

$$\frac{\partial b}{\partial t} = \frac{\dot{m}}{\rho_i} - AN^m b + \frac{(b_r - b) u_b}{l_r}, \quad (2)$$

where ρ_i is the density of ice (so \dot{m}/ρ_i is the volume of ice removed by melt, per unit area and time), u_b is the sliding speed, b_r is the characteristic height of bumps, and l_r the bump spacing. The collapse term is controlled by

Table 1
Variables and Constants Used in This Work

Symbol	Units	Description
b	m	Effective gap-height
q	m^2s^{-1}	Meltwater flux per unit width
\dot{m}	$\text{kgm}^{-2}\text{s}^{-1}$	Melt-rate
i_{eb}	ms^{-1}	Surface meltwater input rate per unit area
ρ_w	kgm^{-3}	Density of water
ρ_i	kgm^{-3}	Density of ice
N	Pa	Effective pressure
p_w	Pa	Water pressure
p_i	Pa	Ice overburden pressure
A	$\text{Pa}^{-n}\text{s}^{-1}$	Viscosity parameter for ice flow
n	-	Ice flow power-law exponent
u_b	ms^{-1}	Ice sliding speed
b_r	m	Characteristic bed bump height
l_r	m	Characteristic bed bump spacing
g	ms^{-2}	Gravitational acceleration
ν	m^2s^{-1}	Kinematic viscosity of water
z_b	m	Bed elevation
h	m	Pressure head
ω	-	Transition to turbulence parameter, 0.001
G	Wm^{-2}	Geothermal flux
L	Jkg^{-1}	Latent heat of fusion of water
τ_b	Pa	Basal shear stress
C	$\text{m}^{-1/2}\text{s}^{1/2}$	Basal friction coefficient (Budd-style sliding)
κ	m^{-1}	Lateral wavenumber
σ	s^{-1}	Growth rate of the perturbation
Σ	-	Dimensionless growth rate constant, 1.0187...
c_p	$\text{Jkg}^{-1}\text{K}^{-1}$	Specific heat capacity of water
T	K	Water temperature
k	$\text{Wm}^{-1}\text{K}^{-1}$	Thermal conductivity of water
Q	Wm^{-3}	Dissipative heating due to water flow
w	m	Channel width
S	m^2	Cross-sectional channel area
Q_c	m^3s^{-1}	Melt-water flux through total channel cross-section
M_c	$\text{kgm}^{-1}\text{s}^{-1}$	Total melt on channel walls per unit length
Ω	m^2s^{-1}	Meltwater input to channel per unit length
f	-	Shape factor accounting for channel aspect ratio

A , the viscosity parameter for the ice, with a power-law exponent n , and N is the effective pressure, the difference between the ice overburden and the water pressure,

$$N = p_i - p_w \quad (3)$$

In Equation 2, we take the closure lengthscale (average cavity width) as equal to b (Schoof, 2010; Sommers et al., 2018; Werder et al., 2013), but other functions of b have also been proposed, such as $l_r/(1 - b/b_r)$ by Kyrke-Smith et al. (2014). Because opening by sliding over bedrock bumps may be less prominent beneath soft-bedded glaciers without large protrusions (Sommers et al., 2023; Zoet & Iverson, 2020), we remove it from our example calculations, but include it in our formal analysis for comparison with I. J. Hewitt (2011).

We take the flux through the water layer q , driven by gradients in the pressure head $h = p_w/\rho_w g + z_b$, to be given by a modified Poiseuille flow,

$$q = -\frac{b^3 g}{12\nu(1 + \omega\text{Re})} \nabla h, \quad (4)$$

where z_b is the bed elevation, ν is the kinematic viscosity of water, $\text{Re} = |q|/\nu = q/\nu$ is the Reynolds number, and ω is a dimensionless parameter describing the frictional resistance in fully developed, turbulent, Darcy-Weisbach flow. The parameter ω therefore also controls the Reynolds number of transition from laminar to turbulent, at $\text{Re} \sim 1/\omega$. There are other possible formulations of this transition to turbulence (e.g., D. R. Hewitt et al., 2018), but we take our expression for consistency with prior work on subglacial hydrology (Hill et al., 2023; Sommers et al., 2018; Zimmerman et al., 2004) and its simple form.

Finally, the melt-rate is found by considering a vertical balance of heat fluxes, so that

$$\dot{m} = \frac{1}{L} (G + |\mathbf{u}_b \cdot \boldsymbol{\tau}_b| - \rho_w g q \cdot \nabla h), \quad (5)$$

where $\dot{m}L$ is the latent heat flux required to melt the ice, G is the geothermal flux, $|\mathbf{u}_b \cdot \boldsymbol{\tau}_b|$ is the frictional heat flux produced by the sliding of the glacier over the bed, and $-\rho_w g q \cdot \nabla h$ is the dissipative heat flux produced by friction in the flow of water itself. We neglect the changes in melting temperature due to pressure variations, which would otherwise appear as a heat source/sink in Equation 5. For the majority of this work, we also assume all the ice is at melting point, and therefore neglect heat fluxes into the ice. In Appendix B3, we describe how to include temperature gradients within the ice in this framework.

We use a Budd-style friction law of the form

$$\tau_b = C^2 N u_b, \quad (6)$$

where C is a friction coefficient, taken as uniform in our simulations. The dependence on the effective pressure N reflects that subglacial hydrology is a strong control on basal traction, although in this paper we do not account for the feedback of N on the sliding speed u_b , which we take as known (e.g., from satellite observations). One could also use a Coulomb sliding law of the form

$$\tau_b = \mu N; \quad (7)$$

as both expressions are linear in N the analysis carries through directly with μ in the place of $C^2 u_b$.

2.2. Subglacial Hydrology in the Absence of Channels

We first calculate the laterally uniform, constant in time solution to our governing equations, representing the distributed system before channels form. The growth rate of the linear perturbations will be determined by this background state.

This solution is given by the profiles of gap height, pressure head, and flux

$$b = \bar{b}(x), \quad h = \bar{h}(x), \quad q = \bar{q}(x), \quad (8)$$

from $x = 0$, the ice divide, to $x = x_r$, the terminus (Figure 1), which solve the governing Equations 1–5 with all time-derivatives and y (lateral) variation ignored.

$$\frac{d\bar{q}}{dx} = \frac{\bar{m}}{\rho_w} + i_{eb}, \quad (9)$$

$$\frac{\bar{m}}{\rho_i} = A\bar{N}^n \bar{b} - \frac{(b_r - \bar{b})u_b}{l_r}, \quad (10)$$

$$\bar{q} = -\frac{\bar{b}^3 g}{12\nu(1 + \omega\bar{q}/\nu)} \frac{d\bar{h}}{dx}, \quad (11)$$

$$\bar{m} = \frac{1}{L} \left(G + |\mathbf{u}_b \cdot \boldsymbol{\tau}_b| - \rho_w g \bar{q} \frac{d\bar{h}}{dx} \right). \quad (12)$$

The ice thickness H (and hence ice overburden pressure $p_i = \rho_i g H$), the bed topography z_b , and the surface meltwater input i_{eb} that drive the subglacial hydrology need to be imposed throughout the modeled domain. For the purposes of the stability analysis, these drivers are also assumed to be laterally uniform and only functions of distance from the terminus.

The boundary conditions are atmospheric pressure $\bar{p}_w(x_r) = 0$ at the terminus, and zero meltwater flux $\bar{q}(0) = 0$ at the divide. With one boundary condition at each end of the domain, we solve these equations using a shooting method: integrating from the terminus toward the divide, starting with the correct imposed water pressure at the terminus and a guess of the outflow flux $\bar{q}(x_r)$, then use a root-finding algorithm to refine the outflow until there is no flux at the ice divide, $\bar{q}(0) = 0$.

An example solution is shown in Figure 2 for constant ice thickness, basal slope, and surface meltwater input (values of parameters given in caption). In this example, the subglacial water flux \bar{q} increases nearly linearly toward the terminus, fed by the constant input of meltwater from the surface and low dissipative heating. This leads to a high pressure head \bar{h} in the interior that decreases rapidly toward the terminus. The gap height \bar{b} initially increases to accommodate the additional meltwater, but drops toward the terminus due to the increased rate of viscous ice collapse as the effective pressure \bar{N} increases.

2.3. Initial Linear Growth Rate of Channels

With these background conditions established, we now introduce small periodic perturbations on top of the background state and calculate whether any wavelengths lead to perturbations that are expected to grow (leading to eventual channelization) or if instead disturbances decay back toward the distributed system found above. We find it convenient to define several parameter groupings, based on the background state, which the behavior of these perturbations, given in Table 2.

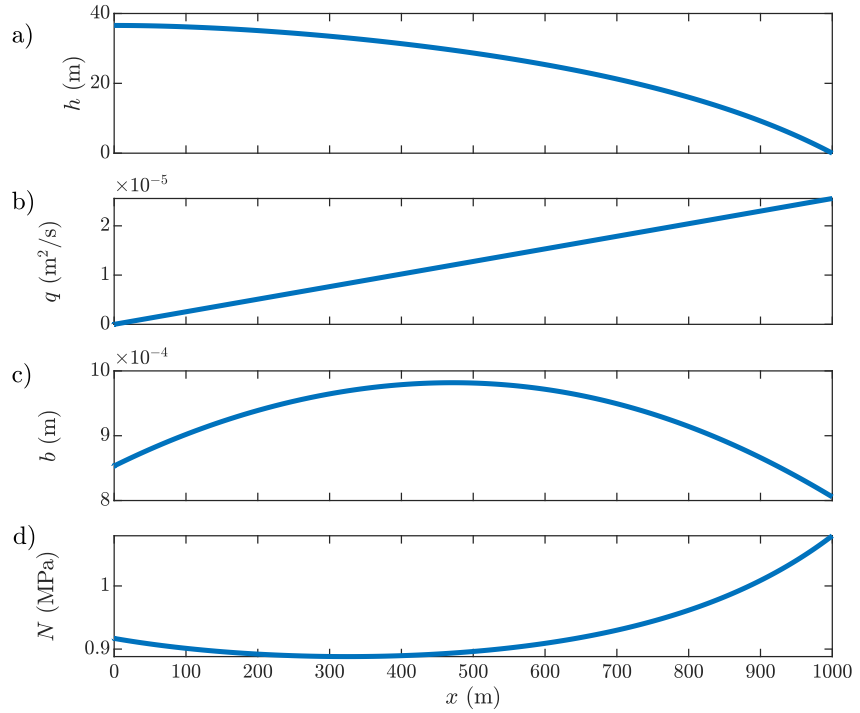


Figure 2. An example of the background solution for (a) laterally uniform pressure head \bar{h} , (b) water flux \bar{q} , (c) gap height \bar{b} , and (d) effective pressure \bar{N} solving Equation 9–12 from the ice divide at $x = 0$ to the terminus at 1 km, in the case of a constant ice thickness of 120 m, distributed meltwater input of 0.8 m/year, and a slope of 0.02 (20 m drop per km) toward the terminus. Gap opening by sliding is ignored in all simulations.

Each possible cross-flow wavelength $\lambda = 2\pi/\kappa$ is associated with a growth rate $\sigma(\kappa)$ and an along-flow structure $\hat{b}(x)$, $\hat{h}(x)$ and $\hat{q}(x)$, which describe how the perturbations evolve between the terminus and the ice divide (Figure 1). The overall perturbed gap height, pressure head, and flux are given by

$$b = \bar{b}(x) + \hat{b}(x)e^{iky+\sigma t}, \quad (13)$$

$$h = \bar{h}(x) + \hat{h}(x)e^{iky+\sigma t}, \quad (14)$$

$$q = \bar{q}(x) + \hat{q}(x)e^{iky+\sigma t}. \quad (15)$$

These expressions are substituted into the governing Equations 1–5, until we obtain a pair of differential equations for $\hat{h}(x)$ and $\hat{b}(x)$, for which $\sigma(\kappa)$ is the eigenvalue allowing all boundary conditions to be simultaneously met. For full details of this procedure, see Appendix B1; the main conceptual steps are given here.

Table 2

Definitions of the Functions of the Background State Used to Streamline the Stability Analysis, and Their Physical Interpretations

Grouping	Definition	Interpretation
K	$\frac{\bar{b}^3 g}{12\nu(1 + \omega \bar{q}/\nu)}$	Hydraulic transmissivity of distributed flow
Q_b	$\frac{-3\bar{b}^2 g}{12\nu(1 + 2 \omega \bar{q}/\nu)} \frac{d\bar{h}}{dx}$	Speed of gap height advection
Q_h	$\frac{\bar{b}^3 g}{12\nu(1 + 2 \omega \bar{q}/\nu)}$	Transmissivity of head perturbations
U	$\frac{\rho_w g \mu_b C^2}{L}$	Sensitivity of frictional melt to pressure
M_b	$\frac{36\nu\rho_w \bar{q}^2 (1 + \omega \bar{q}/\nu)^2}{\bar{b}^4 L (1 + 2 \omega \bar{q}/\nu)}$	Sensitivity of melt-rate to gap height
M_h	$\frac{\rho_w g \bar{q}^2 (2 + 3 \omega \bar{q}/\nu)}{L (1 + 2 \omega \bar{q}/\nu)}$	Sensitivity of melt-rate to pressure gradients

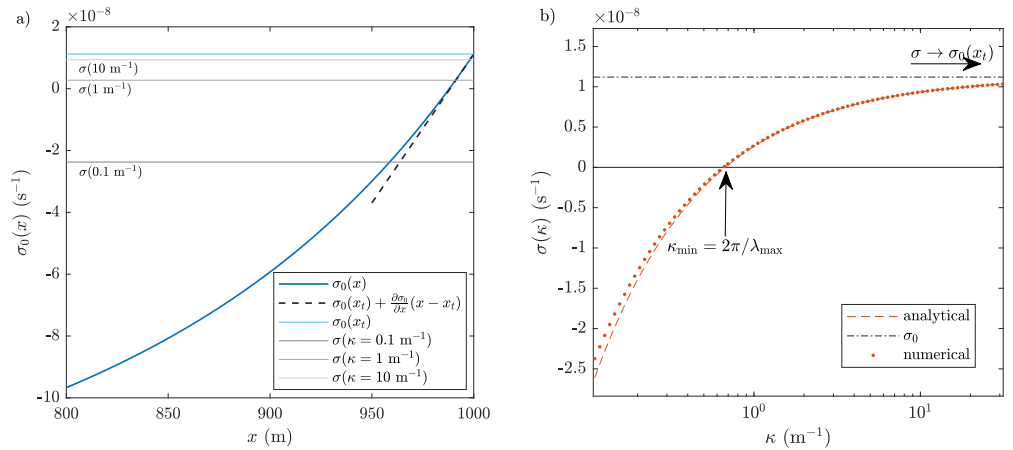


Figure 3. (a) The local balance of melt versus collapse, $\sigma_0(x)$, increases toward the terminus and is eventually is greater than the growth rate for any given wavenumber. The linearization close to the terminus is plotted to show the validity of the analytic approach. (b) Growth rates of perturbations to the background state shown in Figure 2, dots calculated as numerical eigenvalues to Equations 16 and 18 and dashed line calculated analytically per Equation 21. The agreement between the two curves improves as $\kappa \rightarrow \infty$, the limit for which the analytic result is derived. Wavelengths longer than λ_{\max} from Equation 48 are stable, and the shortest wavelengths (largest κ) are the most unstable, tending toward a growth rate of σ_0 per Equation 17.

We find that the perturbation to changes in the motion of the ice-water interface Equation 2 are given by

$$\left(\sigma - \frac{M_b}{\rho_i} + A\bar{N}^n + \frac{u_b}{l_r} \right) \hat{b} = \left(A n \bar{N}^{n-1} \rho_w g \bar{b} - \frac{U}{\rho_i} \right) \hat{h} - \frac{M_h}{\rho_i} \frac{\partial \hat{h}}{\partial x}. \quad (16)$$

This describes how changes in gap height depend on to changes in collapse rate (through changes in pressure and in gap height) and changes in melt-rate (through changes in thermal dissipation from changes in pressure gradients and gap height).

Note that if there were no perturbation to the pressure head, that is, $\hat{h}(x) = 0$, the growth rate would be given by a local, wavelength-independent competition between the tendency of larger gaps promote melt via accommodating faster, more dissipative flow, and their more rapid collapse, which we denote by

$$\sigma_0 = \frac{M_b}{\rho_i} - A\bar{N}^n - \frac{u_b}{l_r}. \quad (17)$$

The shape of $\sigma_0(x)$ for the example of Figure 2 is shown in Figure 3a, and in general is negative (suppressing channelization) close to the ice divide, where M_b is small, but increases toward the terminus. Turning off dissipative heating in the distributed system corresponds setting M_b zero, which completely removes the possibility of instability or channel initiation from regions of initially distributed flow.

Meanwhile, the perturbation to conservation of mass (Equation 1) simplifies to

$$\sigma \hat{b} = -\frac{\partial}{\partial x} \left(Q_b \hat{b} - Q_h \frac{\partial \hat{h}}{\partial x} \right) - K \kappa^2 \hat{h} + \frac{M_b}{\rho_w} \hat{b} - \frac{U}{\rho_w} \hat{h} - \frac{M_h}{\rho_w} \frac{\partial \hat{h}}{\partial x}. \quad (18)$$

This equation describes how the larger, longer wavelength perturbations tend to be stabilized due to the large gradients in pressure head required to sustain flow into them (compare to the similar stabilization by mass conservation noted in Brinkerhoff et al., 2016).

Solving for \hat{h} , \hat{b} , and σ as a function of κ is in general only possible numerically given the complex structure of the background state. To do so, for each value of κ , we guess a value of σ , begin with very small \hat{h} and \hat{b} close to the ice divide, then integrate the equations forwards toward the terminus to find $\hat{h}(x_t)$. We then iteratively update the

value of σ until we find a value producing $\hat{h}(x_t) = 0$, pressure at the terminus matching onto atmospheric pressure. These numerically calculated values of $\sigma(\kappa)$ for the example background state of Figure 2 are shown in Figure 3b.

However, we can make further progress and find an explicit expression for the growth rate in the limit of large κ (short wavelengths). In particular, this is the relevant limit for examining the short-wavelength blow-up. Further, Figure 3b shows that the large κ limit turns out to provide a good match to the numerically derived values throughout the range of unstable wavenumbers. Again, details of the calculation can be found in Appendix B1, but the key insight is that the perturbations are confined to a region close to the terminus, where $Q_b(x)$, $K(x)$, and $M_h(x)$ are approximately constant, while $\sigma - \sigma_0(x)$ is small and taken to be a linear function of x . If there are strong gradients in ice overburden pressure, $\sigma_0(x)$ can have a maximum inland of the terminus, requiring a slight modification to the short wavelength analysis, discussed in Appendix B4.

Under these assumptions, we can explicitly calculate the growth rate associated with each wavelength, along with the corresponding shape of the pressure head and gap height perturbations. We find that \hat{b} is localized close to the terminus, given by a re-scaled Airy function of the first kind,

$$\hat{b} = \text{Ai} \left(\left(\frac{\rho_i K \kappa^2 (\partial \sigma_0 / \partial x)}{Q_b M_h} \right)^{1/3} (x_t - x) - \Sigma \right) \quad (19)$$

while the corresponding perturbed pressure head is proportional to the derivative of \hat{b} , and peaks slightly inland of the terminus,

$$\hat{h} = \left(\frac{Q_b}{K \kappa^2} \right)^{2/3} \left(\frac{\rho_i (\partial \sigma_0 / \partial x)}{M_h} \right)^{1/3} \text{Ai}' \left(\left(\frac{\rho_i K \kappa^2 (\partial \sigma_0 / \partial x)}{Q_b M_h} \right)^{1/3} (x_t - x) - \Sigma \right). \quad (20)$$

Here $\Sigma = 1.0187\dots$ is the smallest value at which the Airy function has zero derivative, chosen so that the pressure boundary condition at the terminus is met. Plots of these functions, and their correspondence to numerical simulations of the full system of equations, are shown in Figures 7e and 7f. The growth rate σ of perturbation at a wavelength $\lambda = 2\pi/\kappa$ is given by

$$\sigma = \sigma_0(x_t) - \Sigma \left(\frac{\partial \sigma_0}{\partial x} \right)^{2/3} \left(\frac{Q_b M_h}{\rho_i K \kappa^2} \right)^{1/3}, \quad (21)$$

shown in Figure 3b.

2.4. Interpretation of the Linear Growth Rate

Beyond its agreement with the numerically determined eigenvalues, we note two important properties of Equation 21, plotted in Figure 3b. First, the growth rate increases as $\kappa \rightarrow \infty$, indicating an unphysical breakdown of the governing equations since the shortest wavelengths are the most unstable. This demonstrates why the channels that develop when these equations are simulated numerically always narrow until they are the size of the finest scale resolved. Second, as $\kappa \rightarrow \infty$, $\sigma \rightarrow \sigma_0(x_t)$ from below, so $\sigma_0(x_t)$ is an upper bound on the growth rate of all scales of perturbations. Thus, the sign of $\sigma_0(x_t)$ determines the overall stability of the system. Substituting the form of M_b from Table 2 into expression Equation 17 for σ_0 , and using Equations 10 and 12 to express the melt-rate in terms of the heat sources, we have instability if

$$\frac{2 + \omega |\bar{q}| / \nu}{1 + 2\omega |\bar{q}| / \nu} \rho_w g \bar{q} \left| \frac{d\bar{h}}{dx} \right| > G + |\mathbf{u}_b \cdot \boldsymbol{\tau}_b| + \rho_i L \frac{b_i u_b}{l_r} \quad (22)$$

at the terminus. We can interpret the terms on the right hand side as the types of heating that allow the distributed system to persist, while the terms on the left are the heating that occurs primarily in rapid channel flow. Thus, channels develop when the melt-rate enhancement provided by channelized flow is enough to open up areas of

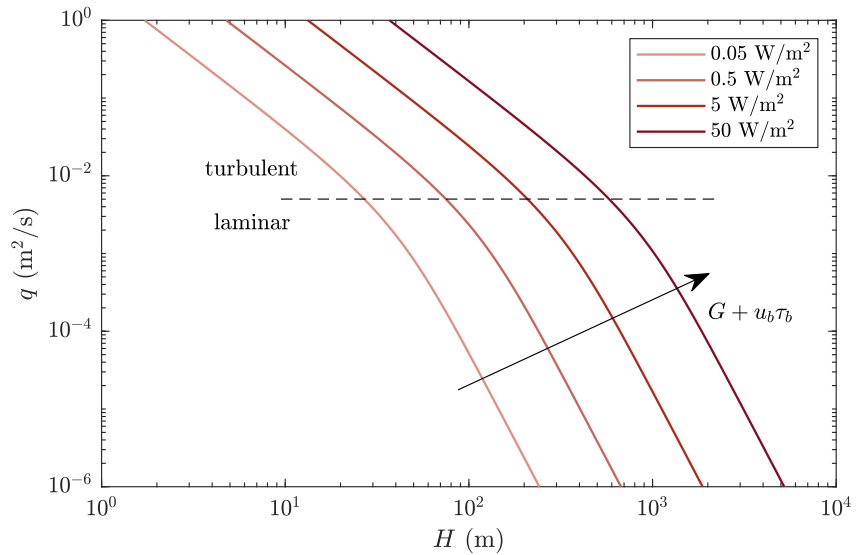


Figure 4. Minimum flux through the terminus (approximately the total volumetric meltwater input, plus melt due to basal heat flux, over the catchment area, divided by the terminus width) needed for channels to initiate, as a function of the ice thickness at the terminus, according to Equation 24, for a range of basal heat fluxes $G + u_b \tau_b$. The break-in-slope corresponds to the laminar-turbulent transition in the hydrology model. Opening by sliding is ignored in this plot, but could be included using Equation 24.

significantly higher gap heights, altering the permeability of the subglacial network and feeding back into reduced water pressure and higher collapse rate away from the channels.

With $\omega = 0$, that is, assuming laminar flow everywhere in the distributed system, Equation 22 agrees with the critical discharge condition of I. J. Hewitt (2011).

$$2\rho_w g \bar{q} \left| \frac{d\bar{h}}{dx} \right| > G + |\mathbf{u}_b \cdot \boldsymbol{\tau}_b| + \rho_i L \frac{b_r u_b}{l_r}, \quad (23)$$

which came from assuming a priori that $\hat{h} = 0$, which we have shown is indeed consistent with the short wavelength limit. Also, since the x scale over which perturbations decay, given by Equation B15, looks like $\kappa^{-2/3}$, and shrinks more slowly than the wavelength in the y direction, $2\pi\kappa^{-1}$, this analysis is consistent with a simpler instability calculation in Schoof (2010) that neglects gradients in x , again highlighting that the behavior is generic despite slightly different formulations of the system.

A more tractable reframing of Equation 22 comes from using Equations 10 and 11 to rewrite the instability criterion in terms of \bar{N} rather than $d\bar{h}/dx$. Since the criterion is evaluated at the terminus, where $\bar{N} = p_i = \rho_i g H$ is just the ice overburden pressure, while \bar{q} can be estimated from inputs and basal melt over the catchment area, this formulation is easier to evaluate for glaciers. We find instability if

$$\frac{12 \times 2^4}{3^3} \frac{\left(1 + \frac{\omega|\bar{q}|}{2\nu}\right)^4 \left(1 + \frac{2\omega|\bar{q}|}{\nu}\right)}{\left(1 + \frac{\omega|\bar{q}|}{\nu}\right)^2} \rho_w \nu \bar{q}^2 \left[\rho_i L \left(A(\rho_i g H)^n + \frac{u_b}{l_r} \right) \right]^3 > \left(G + |\mathbf{u}_b \cdot \boldsymbol{\tau}_b| + \rho_i L \frac{b_r u_b}{l_r} \right)^4, \quad (24)$$

which can be read as a frictional-heat-flux-dependent lower bound on $\bar{q}^2 H^9$ at the terminus, above which channels start to form (Figure 4). The instability initiates when either high effective pressures close down the distributed system, or high basal fluxes promote channelized melt, compared to the terms on the right that promote opening of the distributed system. We demonstrate the power of this stability criterion in predicting the behavior of full numerical simulations of subglacial hydrology in Section 5.1. However, the same stability analysis also predicts a numerical breakdown at short wavelengths, which we turn our attention to next.

3. Inclusion of Heat Transport for Improved Modeling of Channels

The breakdown of existing models of distributed subglacial flow at short wavelengths has been previously noted, and numerically overcome in many ways, from turning off dissipative heating in the distributed system (Werder et al., 2013), imposing a minimum channel width (effectively Sommers et al., 2018), or adding a diffusive term to the gap dynamics (Felden et al., 2023). These approaches seek to minimize the impact of this unphysical behavior; instead, we consider the assumptions that introduce the unphysicality in the first place, providing a more consistent way to regularize the model. We will show, similar to the analysis of Walder (1982), that by considering in more detail the structure of the thermal profile in the water layer, a laterally diffusive term appears (this time in the melt-rate) that provides a physical mechanism for regularization.

To revisit the derivation of the melt-rate in Equation 5, we start from the heat equation

$$\rho_w c_p \left(\frac{\partial T}{\partial t} + \mathbf{u} \cdot \nabla T \right) - k \nabla^2 T = Q, \quad (25)$$

where c_p is the specific heat capacity, k is the thermal conductivity of water and Q is the dissipative heating from the water flow. Since the depth of the water layer is small, we would expect vertical diffusion of temperature to be the dominant mechanism for heat transport. We therefore neglect the advective terms on the left hand side of Equation 25 and ignore the horizontal derivatives in ∇^2 , resulting in

$$-k \frac{d^2 T}{dz^2} = Q. \quad (26)$$

Depth-integrating this equation, applying the geothermal flux and ice-bed frictional heating at the base of the water layer, we find that the heat flux into the ice at the top of the water layer is

$$-k \frac{dT}{dz} \Big|_{z=b} = G + |\mathbf{u}_b \cdot \boldsymbol{\tau}_b| + \int_0^b Q \, dz. \quad (27)$$

Equating this heat flux with the latent heat flux required to melt the ice, $\dot{m}L$, gets us back to Equation 5 for the melt-rate. However, note that the assumption that vertical gradients in temperature dominate over lateral gradients breaks down when the horizontal lengthscale becomes similar to the vertical scale, which happens as the wavelengths become small. Reintroducing lateral heat transport is therefore a plausible way to regularize the short-wavelength behavior.

3.1. Heat Transport Away From Channels

From the above discussion, we see that the missing process in our governing equations is a transport of heat from areas of high heat production (i.e., the dissipative channelized flow) toward colder areas - that is, our modeled channels were infinitely narrow because they could only melt upwards, not into their sidewalls. We therefore need to introduce a term to describe this lateral heat transport, and its impact on the location of melt relative to the location of thermal dissipation.

We begin by calculating the heat flux into the ice, which comes from an integral of the heat equation in the water layer. However, rather than integrating the simpler (Equation 26), which ignores lateral temperature diffusion, we depth-integrate the full steady heat Equation 25 and obtain

$$-k \left(\nabla_H \cdot \int_0^b \nabla_H T \, dz - \nabla_H b \cdot \nabla_H \Big|_{z=b} T \right) = G + k \frac{\partial T}{\partial z} \Big|_{z=b} + |\mathbf{u}_b \cdot \boldsymbol{\tau}_b| + \int_0^b Q \, dz. \quad (28)$$

where ∇_H denotes horizontal gradients, and we have pulled one horizontal derivative outside the integral and generated a boundary term from the spatially varying b .

To then calculate the melt-rate, we balance the latent heat of melting with the heat flux into the ice from the water. Since we are now considering how the melting of sloping interfaces can act to widen channels, we draw a

distinction between \dot{m} , the rate at which the interface appears to move upwards (which we will use in the expression for the motion of the interface, Equation 2), and \dot{M} , the rate at which the interface moves in the direction normal to itself due to melting, where the direction of the normal is

$$\hat{n} = \frac{1}{\sqrt{1 + (\nabla_H b)^2}} \left(-\frac{\partial b}{\partial x}, -\frac{\partial b}{\partial y}, 1 \right). \quad (29)$$

These two rates are geometrically linked via the slope of the interface, $\dot{m} = \sqrt{1 + (\nabla_H b)^2} \dot{M}$. Physically, the heat flux into the interface balances the melting into the interface, so

$$\dot{M}L = -\frac{k}{\sqrt{1 + (\nabla_H b)^2}} \left(\frac{\partial T}{\partial z} - \nabla_H b \cdot \nabla_H T \right). \quad (30)$$

Now, we work to put all of our expressions in terms of b and \dot{m} only, rather than depending on the temperature structure inside the water layer. Since all the ice is assumed to be at the melting temperature, $T(b) = T_m$. Thus if there are horizontal variations in T close to the ice interface, they can be directly related to changes in the distance to that interface, and so by applying the chain rule for differentiation we find

$$\nabla_H|_{z=b} T = -\frac{\partial T}{\partial z} \nabla_H b. \quad (31)$$

We can insert Equation 31 into Equation 30 to write the vertical and horizontal temperature fluxes in terms of the melt-rate and geometry,

$$k \frac{\partial T}{\partial z} = -\frac{\dot{m}L}{1 + |\nabla_H b|^2}, \quad k \nabla_H|_{z=b} T = \frac{\dot{m}L}{1 + |\nabla_H b|^2} \nabla_H b. \quad (32)$$

Inserting these expressions into Equation 28, we obtain

$$\dot{m}L - \nabla_H \cdot \int_0^b k \nabla_H T dz = G + |\mathbf{u}_b \cdot \boldsymbol{\tau}_b| + \int_0^b Q dz. \quad (33)$$

The new term represents the lateral transport of heat via diffusion, so that melt-rate is not only dependent on the local dissipation rate, but also on the heating in neighboring areas. In fact, examining Equation 33, we can still interpret this as a balance of heat fluxes, now including the divergence of horizontal sensible heat fluxes.

We finally make the approximation that horizontal temperature gradients (which in general depend on the detailed structure of the temperature field) are well-approximated by their value close to the ice-water interface (known), and so use Equation 32 for the lateral heat flux everywhere inside the integral. We thus obtain.

$$\dot{m} = \frac{1}{L} \left(G + |\mathbf{u}_b \cdot \boldsymbol{\tau}_b| - \rho_w g \mathbf{q} \cdot \nabla h \right) + \nabla_H \cdot \left(\frac{b \dot{m} \nabla_H b}{1 + |\nabla_H b|^2} \right), \quad (34)$$

$$= \dot{m}_0 + \nabla_H \cdot \left(\frac{b \dot{m} \nabla_H b}{1 + |\nabla_H b|^2} \right) \quad (35)$$

This is the same as our original melt-rate Equation 5, but with a new, non-local, melt-diffusion term that allows areas of high local heat fluxes to also cause melting in their surroundings. We still only need to simulate the gap height, pressure head, and melt-rate, so Equation 34 can be used with Equations 1–4 to simulate subglacial hydrology exactly as before, although now \dot{m} appears on both sides of Equation 34. This structure requires a slightly altered numerical solution approach, described in Section 4.

The term is similar in structure to the gap-height diffusion term introduced in Felden et al. (2023), with two key differences. First, the full melt-rate is included in the diffusivity here, rather than, as in SUHMO,

$$D = \frac{b}{\rho_i L} (-\rho_w g \mathbf{q} \cdot \nabla h), \quad (36)$$

only the dissipative contribution to the melt-rate. This distinction is less important in regions with high basal water flux, but more significant where geothermal flux dominates. Second, as a structural difference, it appears directly in the expression for the melt-rate, versus in Felden et al. (2023), where the gap-height diffusion term is only used to regularize one of the evolution equations for b , with

$$\frac{\partial b}{\partial t} = \frac{\dot{m}_0}{\rho_i} + \beta u_b - AN^n b + \nabla \cdot (D \nabla b). \quad (37)$$

However, the precedent set by their work gives confidence that a diffusional term of this nature is sufficient to dampen the short-wavelength blow-up, as we show in the next section. The linearized analysis will also confirm that the melt-diffusion term in Equation 34 reassuringly agrees with the form found from the full linearized analysis Equation B24.

3.2. Recovery of R othlisberger Channel Behavior

When adding lateral heat diffusion to the SHAKTI equations, the width of the channels is no longer grid-size dependent but converges to a finite width (Figure A1). In this section we show that the evolution of these self-selecting features is comparable to the behavior of R othlisberger channels in models for which separate equations are imposed for the distributed and channelized portions of the domain. Throughout this section we use x to denote the along-channel, and y to denote the cross-channel coordinate.

Integrating mass conservation Equation 1 across a channel of width w , we get

$$\frac{\partial S}{\partial t} + \frac{\partial Q_c}{\partial x} = -\frac{\partial q_y}{\partial y} + \frac{\dot{M}_c}{\rho_w} + i_{eb} w, \quad (38)$$

where S is the cross-sectional area of the channel, Q_c is the total flux through the channel, \dot{M}_c is the total melt on the channel wall, $\Omega = -\partial q_y / \partial y$ is the input of meltwater from the distributed system, and $i_{eb} w$ is the input of surface meltwater landing directly in the channel, which we can neglect, to get

$$\frac{\partial S}{\partial t} + \frac{\partial Q_c}{\partial x} = \Omega + \frac{\dot{M}_c}{\rho_w}, \quad (39)$$

along with the integral of gap height evolution Equation 2 which gives

$$\frac{\partial S}{\partial t} = \frac{\dot{M}_c}{\rho_i} - AN^n S. \quad (40)$$

Integrating the melt Equation 34 across the width of the channel, and neglecting heat diffusion in the along-channel direction, we have

$$\dot{M}_c = \frac{1}{L} \left((G + |\mathbf{u}_b \cdot \boldsymbol{\tau}_b|) w - \rho_w g Q_c \frac{\partial h}{\partial x} \right) + \frac{b \dot{m}}{1 + (\partial b / \partial y)^2} \frac{\partial b}{\partial y}, \quad (41)$$

where the final lateral heat flux term is evaluated at the sides of the channel. If we again neglect the background terms (proportional to w) as small compared to the dissipative melting, and drop the lateral heat flux since b and \dot{m} are small at the very edges of the channel, we arrive at

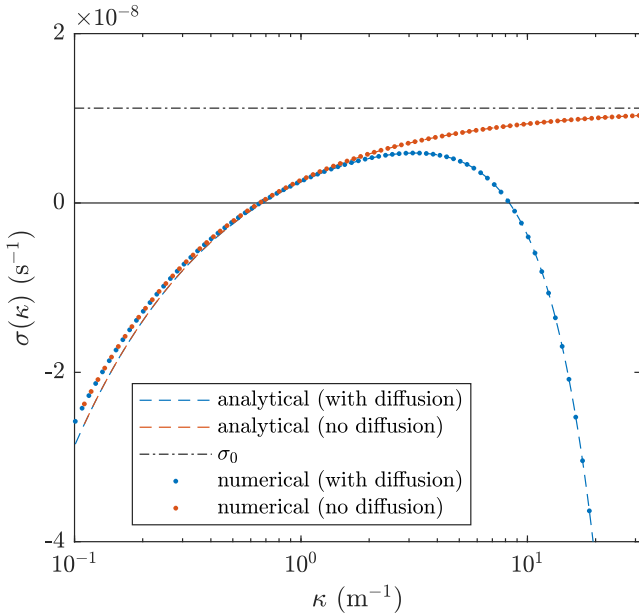


Figure 5. Impact of including lateral temperature diffusion on the growth rates of perturbations. In red, the original model, as in Figure 3b. In blue, the modified growth rates including melt-diffusion: dots are numerical eigenvalues of Equations B25, B26 and dashed line shows the analytic growth rate Equation 45. The shortest wavelengths are now stabilized: there is a most unstable wavenumber given by Equation 46, with growth rate given by Equation 47.

Equations 39, 40, 42 and 44 are exactly the conservation equations expected for Röhrlisberger channels (Werder et al., 2013), and therefore the introduction of lateral heat transport to SHAKTI via the new diffusion term is expected to reproduce the expected channelized behavior.

3.3. Validation of Model Regularization

We now show, via linear stability analysis of the governing equations with lateral heat transport included, that the shortest wavelengths in the system have been stabilized, and therefore we would no longer expect to see infinite narrowing of simulated channels.

The details of the calculation can be found in Appendix B2. We solve for the perturbations in the temperature profile through the water layer, $T = \bar{T}(z) + \hat{T}e^{iky}$, and in the dissipative heating $Q = \bar{Q} + \hat{Q}e^{iky}$, associated with a gap height perturbation $\hat{b}e^{iky}$. We then calculate the perturbation to the melt-rate accounting for lateral heat transport.

The introduction of lateral diffusion of heat modifies the overall growth rate found in Equations 21 to

$$\sigma = \sigma_0(x_i) - \frac{\bar{m}\bar{b}}{\rho_i}\kappa^2 - \Sigma\left(\frac{\partial\sigma_0}{\partial x}\right)^{2/3}\left(\frac{Q_b M_h}{\rho_i K \kappa^2}\right)^{1/3}, \quad (45)$$

which, as shown in Figure 5, is stable at both the largest and smallest wavenumbers.

Importantly, we now have a maximum growth rate at a finite value of κ , since σ decreases quadratically as κ gets large. This indicates that we have regularized the short wavelength singularity. The most unstable wavenumber is at approximately

$$\kappa = \left(\frac{\Sigma\rho_i}{3\bar{m}\bar{b}}\right)^{3/8}\left(\frac{\partial\sigma_0}{\partial x}\right)^{1/4}\left(\frac{Q_b M_h}{\rho_i K}\right)^{1/8}. \quad (46)$$

$$\dot{M}_c = \frac{Q_c}{L} \frac{\partial h}{\partial x}. \quad (42)$$

To find the flow law giving Q_c , we need to link the width of the channel to its height. To find such a scaling relationship, we combine (Equations 2 and 34), ignore opening by sliding (anticipating that $b > b_r$), and take the limit of long, quasi-steady channels by neglecting t - and x - derivatives,

$$0 = \dot{m}_0 - \rho_i A N^m b + \frac{\partial}{\partial y} \left(\frac{\dot{m}b}{1 + (\partial b / \partial y)^2} \frac{\partial b}{\partial y} \right). \quad (43)$$

This is a differential equation for $b(y)$, where \dot{m}_0 also depends on b through q . We do not attempt to solve Equation 43 directly for the shape $b(y)$. Instead, we argue that for large melt-rates, the shape of the channel is set by a balance between dissipation near the center of the channel, and lateral diffusion of heat causing melt into the channel sidewalls. A balance between these terms can only hold if $b \sim y$, and so the width of channels must be comparable to their height. Thus, integrating (Equations 4) in the limit of high Re, we have

$$Q_c = \frac{(g|\nabla h|)^{1/2}}{(12\omega)^{1/2}} \int_{-w/2}^{w/2} b(y)^{3/2} dy = \frac{(g|\nabla h|)^{1/2}}{(12f\omega)^{1/2}} S^{5/4} \quad (44)$$

where f is a shape factor relating the integral of $b^{3/2}$ across the width of the channel to $S^{5/4}$, since both scale like $b^{5/2}$. The shape factor will depend on the exact shape of the channel (e.g., for exactly semi-circular channels, $f \approx 1.44$).

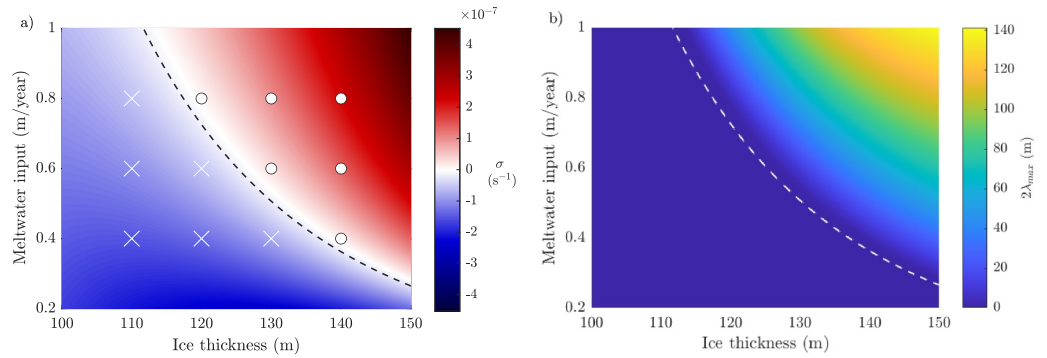


Figure 6. (a) Effect of varying meltwater input and ice thickness on three metrics of channelization. Dashed line gives the approximate stability criterion Equation 24, where we use total meltwater input and geothermal melting only to estimate of flux at the terminus. Color shows σ , the maximum growth rate predicted by Equation 47, using a 1D calculation of \bar{q} that includes dissipative melt at the bed. Outcomes from the full numerical simulations are superimposed - crosses indicate no channels, circles indicate channels developed. When the maximum predicted growth rate is positive, channelization is indeed observed. The boundary predicted by Equation 24 lies just inside the stable regime according to Equation 47 due to the impact of melt-diffusion, which is not considered in Equation 24. (b) Predicted minimum mesh side length needed to resolve instability, equal to $2\lambda_{\text{max}}$, from Equation 48. Regions without instability are shown as 0. Channels are most vulnerable to numerical suppression close to the margin of stability, when the required mesh size gets small.

While this wavelength is small (comparable to the thickness of the water layer), the channels produced by the modified system of equations should no longer be infinitely narrow. The maximum growth rate is slightly reduced by the diffusive effects to

$$\sigma = \sigma_0(x_t) - 4 \left(\frac{\bar{m}\bar{b}}{\rho_i} \right)^{1/4} \left(\frac{\Sigma}{3} \right)^{3/4} \left(\frac{\partial \sigma_0}{\partial x} \right)^{1/2} \left(\frac{Q_b M_h}{\rho_i K} \right)^{1/4}, \quad (47)$$

as can be seen in Figure 5, the maximum growth rate is somewhat less than σ_0 . However, the stability criterion (Equations 24) based only on $\sigma_0(x_t)$ still holds to good approximation (e.g., Figure 6a).

We have demonstrated that our improved set of governing equations produce wavelength selection, and thus should not be prone to the previous unphysical breakdown at small scales. We next perform numerical simulations of these equations to demonstrate both the validity of our analysis and to illustrate the power of the linearized analysis for predicting the behavior of subglacial hydrology without resorting to full numerical simulation.

4. Simulation Results

We implemented the SHAKTI governing equations, with the additional melt-diffusion term, in the adaptive-mesh PDE solver Basilisk (Popinet, 2013–2024) using the inbuilt Poisson solver to calculate the pressure head and flux, and an explicit fixed time-step forward Euler method to update the gap height. The subglacial geometry and melt-rate are only updated during the explicit time-step, and kept at this value during the following Poisson solve routine. For ease of implementation, we used the value of melt-rate from the previous timestep to calculate the lateral heat transport term appearing in Equations 34. The mesh adaptation and interpolation are handled by the adapt routine of Basilisk. The adaptive mesh allowed us to locally reach much higher resolutions than possible in the original ISSM implementation of SHAKTI (Sommers et al., 2018).

We perform the majority of our simulations in the same idealized test geometry as Sommers et al. (2018), a 1 km square domain with uniform ice thickness and slope of 0.02 toward the outflow boundary, at which we impose atmospheric pressure, while the other three sides of the domain are no-flux boundaries. We focus on a test case that is close to the stability boundary, 120m-thick ice with distributed meltwater input of 0.8 m per year throughout the domain (matching the scenario presented in Figures 2, 3 and 5 of this paper). The simulations are initiated with a gap height in the range 0.9–1 mm, independently selected from a uniform random distribution for each mesh cell. The simulations rapidly converge to something close to the laterally uniform base state, with small deviations away from this localized near the terminus.

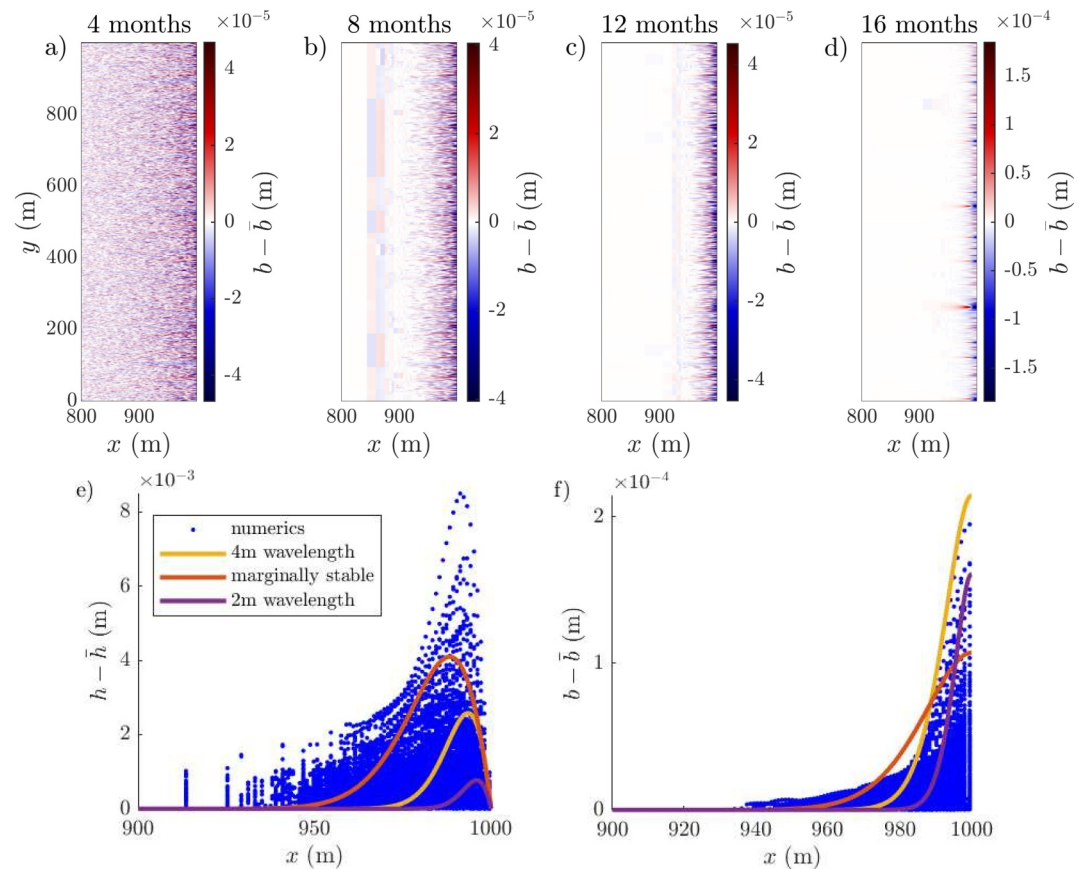


Figure 7. (a–d), evolution of the deviation in gap height away from the width-averaged value. Initially, the deviation is due to the random noise introduced everywhere in the domain. The perturbations with the largest lengthscales are stable and thus decay away, leaving only the narrow fluctuations close to the terminus. These small-scale perturbations are unstable and grow into channels propagating back into the interior of the domain. The larger scale blocks seen ~ 200 m from the terminus are artifacts from mesh adaptation. (e–f), comparison between the numerical deviation from average pressure head (e) and gap height (f) at 12 months, and the Airy eigenfunctions for a range of unstable wavelengths. The relative size of \hat{h} and \hat{b} is set by Equation 20, and thus the agreement in both amplitude and shape give additional confidence in the analytic results. The persistence into the interior and the somewhat larger $h - \bar{h}$ than predicted can be attributed to longer wavelength, stable modes that are still decaying away.

4.1. Channel Development

We ran simulations varying meltwater inputs between 0.4 and 0.8 m per year and ice thicknesses between 110 and 140 m. Figure 6a records whether or not channels developed after a year of simulation time. The outcome is well-predicted by our stability criterion (Equations 24).

For the case of 0.8 m per year input, 120m-thick ice, the deviation of gap height away from the laterally averaged value is shown in Figure 7. The gap height in the interior converges to the distributed state, while the perturbations close to the margins grow, before merging to form channels. These channels then propagate back into the interior of the domain. A video of the full timeline of channel evolution is available in the supplement.

4.2. Minimum Resolution Requirement

For coupled ice-hydrology models, we would ideally simulate the subglacial hydrology at the same resolution as that of ice flow, that is, on a grid at the kilometer scale, but this is not plausible with our model, as the resolution of numerical simulations can dramatically impact the behavior of the simulated water flow. Since long wavelengths are always stable (Figures 3b and 5) due to the scale of pressure gradients they induce, simulations on a coarse grid may appear stable even in a regime where instability is expected. The maximum unstable wavelength,

$$\lambda_{\max} = \frac{2\pi}{\Sigma^{3/2}} \left(\frac{\rho_i K}{Q_b M_h} \right)^{1/2} \frac{\sigma_0(x_i)^{3/2}}{\partial \sigma_0 / \partial x}, \quad (48)$$

found by setting the growth rate in Equations 21 to 0, controls the scale above which any disturbances decay away. If the smallest scales resolved by the simulation are larger than this wavelength, the numerical simulation will not produce instability, since the only drivers of channelization would occur on smaller scales than can be resolved. Thus, we find channels can be suppressed numerically in situations where a physical balance would predict instability. This results in the persistence of an inefficient drainage system, leading to an overestimate of basal water pressure (Figure 8). In a coupled simulation, this numerical artifact would therefore lead to an overestimate of sliding velocities throughout this region.

To illustrate this effect, we simulated the same idealized test case across a range of maximum grid resolutions. We deliberately chose a configuration that was only just unstable, leading to a fairly small value of $\lambda_{\max} = 9.52$ m according to (Equations 48). Basilisk requires the number of gridpoints to be a power of 2, so for our 1 km domain we tested meshes from $1000/2^6 = 15.625$ m to $1000/2^{10} = 0.977$ m. Channelization was suppressed by the 15.6 and 7.81 m meshes, but occurs with the 3.91 m mesh and smaller, since at this mesh size and below at least two grid points fit within an unstable wavelength and an unstable oscillation can be simulated (Figure 8).

Although simulating a full glacier at a resolution below 4 m is currently unreasonable, Figure 6b shows that the minimum resolution required to capture the instability grows rapidly, to a scale of hundreds of meters, as we move away from the stability boundary. Thus, caution is only needed close to the onset of channel formation. Even a relatively low-resolution model will predict channelization if the system is unstable enough.

However, Figure 8 also demonstrates that even when channel formation is captured, the inland extent and spacing of the channels remain grid-dependent until the width of the channels is well-resolved. Without melt-diffusion, channels remain one grid-cell wide (cf. Felden et al., 2023) and the channel spacing never converges. Including the melt-diffusion term allows for finite width channels and for the channel distribution to converge, but requires resolutions higher than the width of channels (cf. Appendix A1).

5. Discussion

5.1. Channel Initiation is a Predictable Linear Process

Both the growth rate (Equations 45) and the stability criterion (Equations 24) successfully predict whether or not channels develop in numerical simulations, over a range of surface meltwater inputs and ice thicknesses (Figure 6a). Channelization occurs if the flow-rate within the channels is high, especially if strong creep-closure elsewhere prevents water from leaving through the distributed system. Thus, we see channels form when the rate of meltwater input is large (high dissipative heating and local melt keeps the channels open) and when the ice sheet is thicker (ice overburden pressure promotes closure and tamps down on the distributed system). The stability criterion (Equations 24) depends only on the glacier geometry and estimates of net surface meltwater input within the catchment area. As it can be quickly evaluated, it provides a quick estimate of the character of subglacial flow to compare with spatio-temporal patterns of glacier velocity, without running a full numerical simulation.

Beyond the stability criterion, the structure of the variations in gap height and water pressure are also well-predicted by the stability analysis. In the unstable cases, the initial perturbations first develop close to the margin of the ice sheet, at a wavelength comparable to the most unstable mode (Equations 46). The along-flow structure of the growing gap-height and water-pressure perturbations match the shapes predicted by the Airy eigenfunctions (Figure 7), with large variability close to the margins, decaying inland. This suggests that channels are more likely close to termini (in agreement with observations and simulations; Werder et al., 2013; Poinar et al., 2019) as they initiate in this near-terminus region of large pressure perturbations and then propagate inland.

A potential implementation would be to apply the stability criterion over a range of catchment areas across Greenland, under both summer and winter conditions. From this one could assess if basal melt leads to persistent wintertime channels, if distributed drainage networks remain through summer, or if channels are expected to develop during the melt season. Relating these predicted behaviors to the amplitude of the seasonal velocity response would then provide a strong test for our model. In the opposite direction, we could assess how much

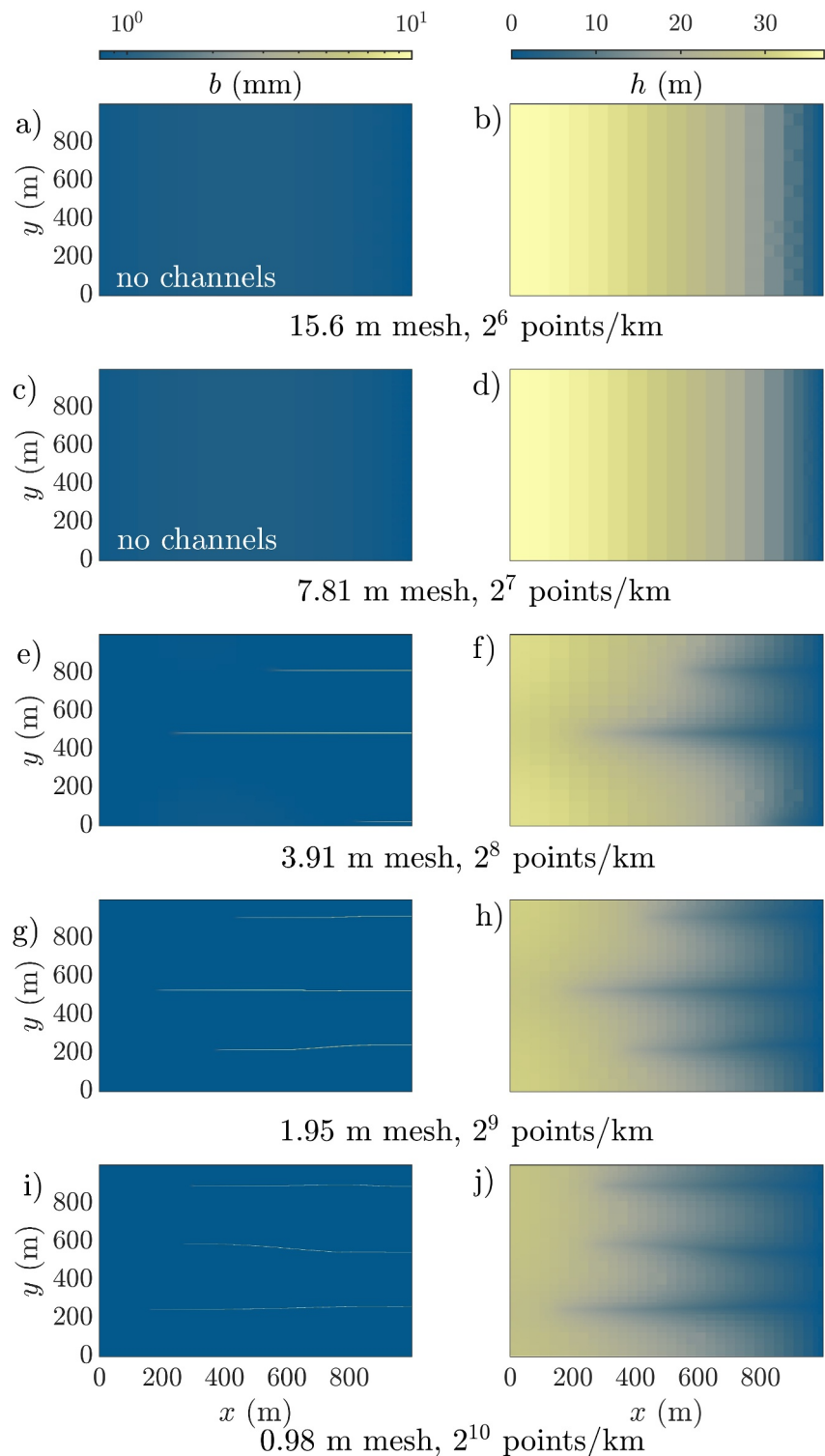


Figure 8. The impact of varying resolution on the state of the simulated subglacial hydrology after 10 years of simulation time. Minimum mesh size halves with each plot from top to bottom. Left panels show gap height b (in mm, log colorscale), and right the corresponding pressure head h (in m). The channels are regions of lower water pressure compared to the surrounding regions, pulling meltwater from their surroundings and funneling it toward the margin (right hand side of domain). Large meshes suppress channelization and result in higher inland water pressures. The final channel spacing, unrelated to the linear initiation, emerges as neighboring channels compete and migrate inland (video in Supporting Information S1).

meltwater input is required to change the seasonal flow of a glacier, or if current wintertime channels minimize the potential impact of any future seasonal melt on accelerating ice velocity. This is particularly relevant not only for Greenland, but also for mountain glaciers that experience seasonal melt, and for the future of the Antarctic ice sheet as the area warms.

5.2. Strong Non-Linearity of Channel Propagation

As the perturbations develop and propagate inland, they become non-linear features: large, distinct channels surrounded by almost fully drained areas of distributed flow, far from a small perturbation in sheet depth. These features evolve according to the equations for Röthlisberger channels (see Section 3.2). The interactions between neighboring channels involve complex, long-range competition for the meltwater delivered from the surface. Channels that lose out on meltwater suddenly collapse, with winning channels growing rapidly into the vacated space (video in Supporting Information S1). As such, the dynamics that govern the evolution of channel spacing cannot be explained using linear stability analysis. The most unstable wavelength, despite its importance to the early time patterns of channels, is not visible in the final configuration of the subglacial hydrology.

Predicting the number of channels in a catchment area, their average spacing, and net effect on the subglacial water pressure remains challenging. From an analysis of the pressure distribution around a single, non-evolving channel, I. J. Hewitt (2011) suggested that the spacing of channels should be similar to their length. Our final configurations show a somewhat smaller spacing (e.g., in Figure 8, around one third of their length). Overall, being able to predict the evolution of average properties of the subglacial system (such as channel spacing and effective pressure) without simulating individual channels is a goal for reduced modeling. Numerical simulations can provide an important inspiration for the development of such models, but are vulnerable to producing numerical artifacts, an example of which we discuss below.

5.3. Relevance to More Realistic Scenarios

The configuration we study here is idealized in two main ways: the simple, laterally uniform geometry, and the meltwater input that is kept constant in time. In the simulations shown in Figure 8, the meltwater input is kept constant over a timescale of years to allow the channels to fully develop to a steady configuration, a poor representation of seasonal melt for Greenland and mountain glaciers. In part, this is due to our focus on conditions close to marginal stability, where the growth rates of instabilities are small. In more unstable configurations, the growth rate (Figure 6) is orders of magnitude larger, so channels develop on a timescale of weeks. This illustrates that it is not only the sign of the maximum growth rate (Equation 47), but also its magnitude, that controls whether large channels develop during a melt season. To explain the seasonal patterns of subglacial hydrology, we would need to look at the total time-integrated growth rate with varying meltwater input, to assess if and when the first channel-sized features appear. We leave this for future work.

Our simplified geometry allows us to perform stability analysis using a background state that is uniform across the width of the terminus, leading to the appearance of self-selecting, randomly distributed perturbations across the domain. The basal topography of real glaciers and ice streams is heterogeneous at a range of scales, guiding both the location of channel initiation and the pathways in the final channel configuration (e.g., de Fleurian et al., 2018; Dow, 2022; Hiester et al., 2016). However, our analysis still highlights the fundamental competition between channelizing melt and viscous ice collapse that governs the question of channelization. Thus, we may still be able to predict which glaciers are likely to feature an efficient subglacial network based on a representative assessment of criterion (Equation 24) at the glacier terminus.

As a demonstration, we ran SHAKTI in the ISSM framework on a domain including Russell Glacier (RG) and Isunnguata Sermia (IS) in Southwest Greenland under winter (no surface meltwater input) conditions (per Sommers et al., 2023), using geometry from BedMachine v4 (Morlighem et al., 2017) and velocities from MEASUREs (Joughin et al., 2018). As shown in Figure 9, a channel forms under IS but not under RG. We compare this to the maximum growth rate of instabilities based on 1D profiles down the midlines of each glacier (dashed lines on Figure 9). We find a positive growth rate of $1.33 \times 10^{-7} \text{ s}^{-1}$ at IS, consistent with channel development. At RG, which has thinner ice at the terminus, the maximum growth rate is $-6.79 \times 10^{-8} \text{ s}^{-1}$. The negative value indicates that distributed flow is indeed expected during the winter. These results indicate that linear stability analysis can provide a characterization of subglacial hydrology even in more complex domains.

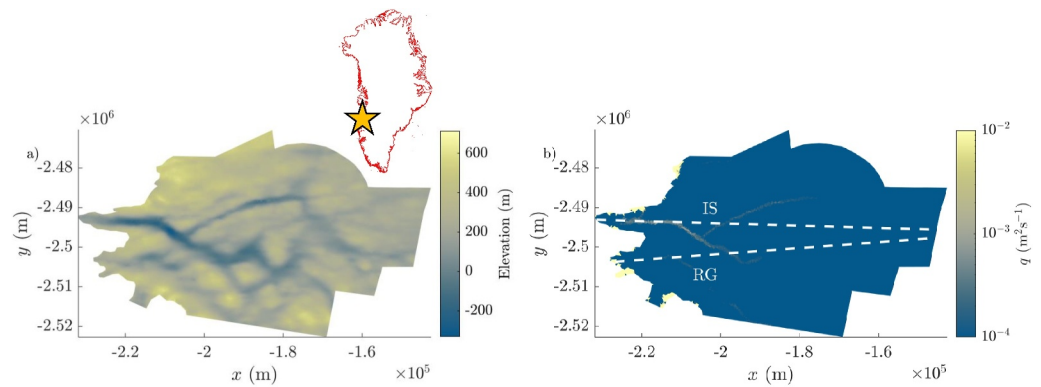


Figure 9. (a) Topography beneath Russell Glacier (RG) and Isnunnguata Sermia (IS). The inset shows the location in southwest Greenland. (b) Subglacial water flux beneath RG and IS under winter conditions, as simulated in SHAKTI. A channel develops beneath IS following the lows in basal topography (Morlighem et al., 2017). Dashed lines indicate the profiles of topography and ice thickness used for the stability calculations.

6. Conclusions

To better understand both the channelization of subglacial hydrology and numerical models thereof, we have performed a full linear stability analysis of distributed subglacial flow, finding a stability criterion and the growth rates of different scales of perturbations.

We confirmed the existence of a short-wavelength blow-up in the original model of distributed water flow, under which channels always narrow unphysically to the smallest scale of the simulation. We demonstrated that consistent, convergent simulated behavior can be achieved through the re-introduction of lateral temperature diffusion to the model, and have derived a melt-rate diffusion term to parameterize this effect, allowing for its smooth integration into existing modeling frameworks. We also showed that long wavelength perturbations are always stabilized, due to the large pressure gradients they induce, and thus derived a minimum resolution requirement (Equation 48) below which numerical models are unable to resolve the onset of channelization.

Importantly, we have demonstrated that channels initiate when the enhanced melt due to heat produced by flow inside a channel overwhelms the balance between geothermal and viscous ice collapse that controls the distributed flow network. This criterion (Equation 24) provides a rapid estimate of when and where an efficient subglacial system is expected to form, and thus opens a path for understanding the seasonal trends of glacier velocity and their possible changes in a warming climate, without recourse to a full numerical model. Application of this efficient calculation holds high potential for interpreting and projecting future changes in ice velocity caused by changes in water flow beneath glaciers and ice sheets.

Appendix A: Validation of Basilisk Implementation

A1. Comparison to SUHMO: Single Channel From a Moulin

We implemented the same channelizing test case as in SUHMO (Felden et al., 2023), a 64 m domain with a bedslope of 0.02 (20 m drop per km) and a slab of ice of constant 500 m thickness. A moulin delivering $30\text{m}^3\text{s}^{-1}$ of water is located 16 m from the margin with a Gaussian profile in space. The moulin input is gradually increased in time, from 0 at time $t = 0\text{s}$ to the maximum value after about a month, and the simulation proceeds until steady state is reached.

Similarly to the SUHMO results, the channel converges toward a fixed height and width with increasing numerical resolution (Figure A1). We produce a wider, less tall channel than in SUHMO (6 vs. 3 m wide, 0.9 vs. 1.5 m high) due to the higher diffusivity that includes the geothermal flux, promoting enhanced widening rates in the channels. Without diffusion, the channel height and width are grid-size dependent (Figure A2).

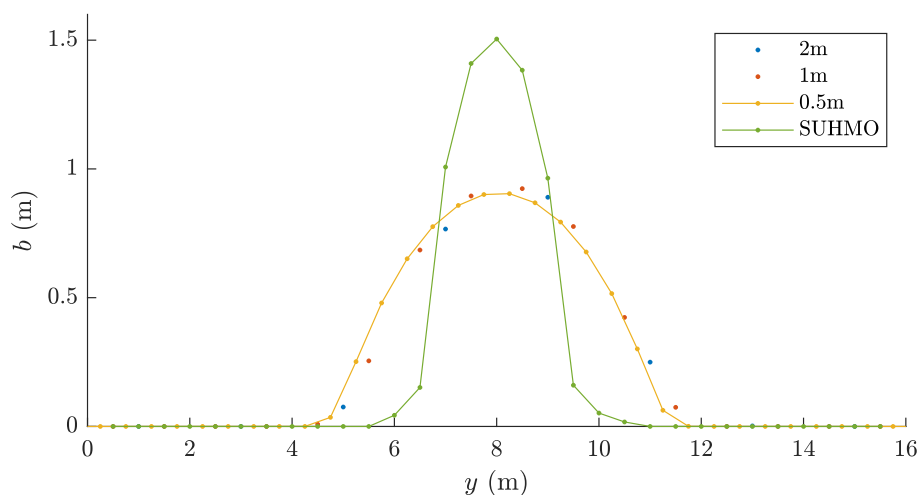


Figure A1. Gap height b at a transect 10 m inland of the margin, when a large moulin is located 16 m inland of the margin. We see convergence in channel width and height with increasing resolution. The same example in SUHMO produces a taller, narrower channel, as expected.

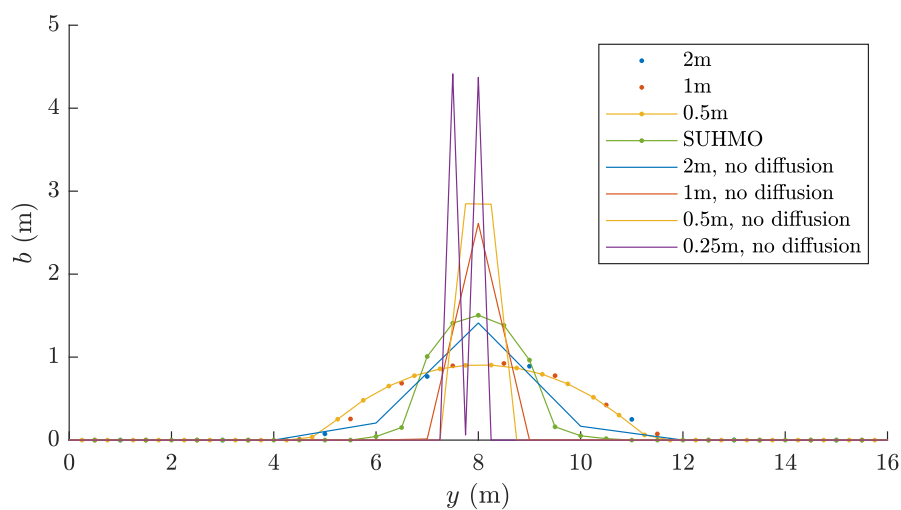


Figure A2. The same moulin configuration as in Figure A1, with the addition of the results of the original SHAKTI equation (without melt-diffusion). The original model results do not converge with increasing mesh resolution.

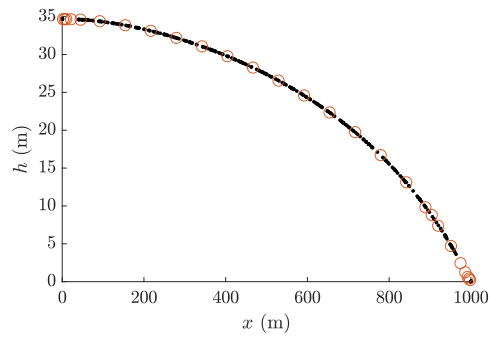


Figure A3. Pressure head from the ISSM (black dots) and Basilisk (red circles) implementations of SHAKTI show complete agreement throughout the domain in the distributed case (with 0.6 m/year of meltwater input, 120 m thick ice, after 10 years of simulation time.).

A2. Comparison to ISSM

We simulated the 120 m ice, 0.6 m/year melt configuration in both the ISSM Version 4.21 and Basilisk implementations of SHAKTI. This case is predicted not to channelize (Figure 6), providing a test of the Poisson solver, as both should converge toward the same laterally uniform state. Indeed, we found the same distributions of pressure head and gap height in both implementations (Figure A3).

We then tested 130 m thick ice with 0.8 m/year of meltwater, which as predicted results in channels in both the ISSM and Basilisk implementations (Figure A4). Both simulations developed two large channels and one small channel. The location of the channels differs between simulations, which is to be expected from the randomly seeded initial perturbation.

These two experiments give confidence that our Basilisk implementation of the SHAKTI governing equations is correct.

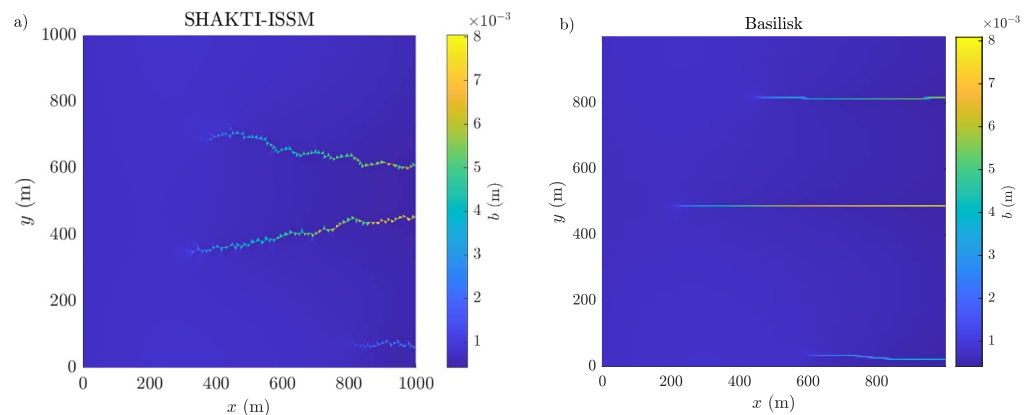


Figure A4. Channels that developed in a 1 km square domain, with 0.8 m/year of meltwater input, 130 m thick ice, after 10 years of simulation time. (a) With the ISSM implementation of SHAKTI, using an average mesh side length of 5 m (minimum 3.84 m), (b) with the Basilisk implementation of SHAKTI, and a minimum mesh size of 3.91 m.

Appendix B: Details of the Linear Stability Analysis

B1. Original System of Equations

We start from the governing Equations 1–5, and insert the perturbed gap height, pressure head, and flux expressions

$$b = \bar{b}(x) + \hat{b}(x)e^{iky+\sigma t}, \quad (\text{B1})$$

$$h = \bar{h}(x) + \hat{h}(x)e^{iky+\sigma t}, \quad (\text{B2})$$

$$\mathbf{q} = \bar{\mathbf{q}}(x) + \hat{\mathbf{q}}(x)e^{iky+\sigma t}. \quad (\text{B3})$$

We work in a laterally infinite and uniform domain, so all values of κ are possible. Since there is no y or t dependence in the background state, each mode of perturbation has the same values of κ and σ across all variables.

Substituting these expressions into the equation for the flux (Equation 4), and retaining only the terms linear in the perturbations, we find that the perturbed flux can be expressed in terms of the background state and the gap and pressure head perturbations as

$$\hat{\mathbf{q}} = -\frac{\bar{b}^3 g}{12\nu(1 + \omega|\bar{q}|/\nu)} \left[\frac{1 + \omega|\bar{q}|/\nu}{1 + 2\omega|\bar{q}|/\nu} \left(\frac{3\hat{b}}{\bar{b}} \frac{d\bar{h}}{dx} + \frac{\partial\hat{h}}{\partial x} \right) \hat{\mathbf{x}} + ik\hat{h}\hat{\mathbf{y}} \right] \quad (\text{B4})$$

and the perturbation to the divergence in flux is therefore

$$\widehat{\nabla \cdot \mathbf{q}} = \left(\frac{\partial}{\partial x} \left[\frac{-\bar{b}^3 g}{12\nu(1 + 2\omega|\bar{q}|/\nu)} \left(\frac{3\hat{b}}{\bar{b}} \frac{d\bar{h}}{dx} + \frac{\partial\hat{h}}{\partial x} \right) \right] + \frac{\bar{b}^3 g \kappa^2}{12\nu(1 + \omega|\bar{q}|/\nu)} \hat{h} \right). \quad (\text{B5})$$

For convenience in the following analysis, we give names to these functions of the base state (Table 2), and write

$$\widehat{\nabla \cdot \mathbf{q}} = \frac{\partial}{\partial x} \left(Q_b \hat{b} - Q_h \frac{\partial\hat{h}}{\partial x} \right) + K \kappa^2 \hat{h}. \quad (\text{B6})$$

The functions $Q_b(x)$, $Q_h(x)$, and $K(x)$ are always positive, and describe how easily variations in pressure and gap height are transported in different regions of the distributed system.

Substituting the expression for the flux into the melt-rate (Equation 5), we find that melt-rate perturbations can also be expressed in terms of pressure head and gap height,

$$\hat{m} = \frac{\rho_w g}{L} \left(-u_b^2 C^2 \hat{h} - \frac{1 + \omega|\bar{q}|/\nu}{1 + 2\omega|\bar{q}|/\nu} \bar{q} \frac{3}{\bar{b}} \frac{d\bar{h}}{dx} \hat{b} - \frac{2 + 3\omega|\bar{q}|/\nu}{1 + 2\omega|\bar{q}|/\nu} \bar{q} \frac{\partial\hat{h}}{\partial x} \right). \quad (\text{B7})$$

Again, we give names to these functions of the base state (Table 2), so

$$\hat{m} = -U(x)\hat{h} + M_b(x)\hat{b} - M_h \frac{\partial\hat{h}}{\partial x}. \quad (\text{B8})$$

here, $U(x)$ describes the impact of pressure variations on friction at the glacier bed, $M_b(x)$ describes how sensitive the melt-rate is to changes in gap height, and $M_h(x)$ describes how changes in pressure gradients impact the melt-rate through changes in flow rate. Again, all these functions are defined so as to be positive quantities (the sensitivity of melt-rate to the different variables). Turning off dissipative heating in the distributed system corresponds to a case where M_h and M_b are both zero, which we shall see immediately removes the possibility of instability or channel initiation in these regions.

Inserting these results into the motion of the ice-water interface (Equation 2), we obtain a first equation linking changes in water pressure to the growth rate of the gap height perturbation,

$$\left(\sigma - \frac{M_b}{\rho_i} + A\bar{N}^n + \frac{u_b}{l_r}\right)\hat{b} = \left(A_n\bar{N}^{n-1}\rho_w g \bar{b} - \frac{U}{\rho_i}\right)\hat{h} - \frac{M_h}{\rho_i} \frac{\partial \hat{h}}{\partial x}. \quad (\text{B9})$$

In the limit where pressure perturbations played no role and $\hat{h} = 0$, the growth rate would be given by

$$\sigma_0 = \frac{M_b}{\rho_i} - A\bar{N}^n - \frac{u_b}{l_r}. \quad (\text{B10})$$

Meanwhile, the perturbation to conservation of mass (Equation 1) simplifies to

$$\sigma \hat{b} = -\frac{\partial}{\partial x} \left(Q_b \hat{b} - Q_h \frac{\partial \hat{h}}{\partial x} \right) - K\kappa^2 \hat{h} + \frac{M_b}{\rho_w} \hat{b} - \frac{U}{\rho_w} \hat{h} - \frac{M_h}{\rho_w} \frac{\partial \hat{h}}{\partial x}. \quad (\text{B11})$$

This equation describes how the larger, longer wavelength perturbations tend to be stabilized due to the large gradients in pressure head required to sustain flow into them (compare to the similar stabilization by mass conservation noted in Brinkerhoff et al., 2016)

Together, the pair of differential equations for \hat{h} and \hat{b} (Equations B9, B11) at a particular value of κ has the structure of an eigenfunction problem, where the growth rate $\sigma(\kappa)$ is the eigenvalue, that is, the only value of σ that allows all the boundary conditions to be simultaneously met. The boundary conditions are $\hat{h}(0) = 0$ (no pressure variations at the terminus, as the outflow pressure is the same everywhere); the decay of \hat{h} and \hat{b} toward the ice divide (inspecting the structure of the differential equations, this turns out to be a single condition); and finally since both equations are linear and we can multiply both $\hat{b}(x)$ and $\hat{h}(x)$ by any constant value without affecting the structure of the solution, we impose $\hat{b}(0) = 1$ for convenience.

In the limit of large κ (short wavelengths), we can make further analytic progress. We anticipate that variations in the pressure head will be small, $\hat{h} \ll 1$, so that the $\kappa^2 \hat{h}$ term in Equation B11 remains balanced. We therefore also expect $\sigma - \sigma_0 \ll 1$ as we will be close to the $\hat{h} = 0$ solution to Equation B9, and so find that $\partial \hat{h} / \partial x \ll \hat{b}$. Finally, in order to keep all the boundary conditions we must preserve the \hat{b} -derivative in Equation B11, which implies that $x \ll 1$. Under these assumptions, Equation B11 becomes

$$\hat{h} = -\frac{1}{K\kappa^2} \frac{\partial(Q_b \hat{b})}{\partial x}, \quad (\text{B12})$$

which, substituted into Equation B9, yields

$$\frac{\partial^2(Q_b \hat{b})}{\partial x^2} = \frac{\rho_i K \kappa^2}{M_h} (\sigma - \sigma_0) \hat{b}, \quad (\text{B13})$$

a single second order differential equation for \hat{b} .

With $x \ll 1$, our perturbations are confined to a boundary layer close to the terminus, so we can approximate $Q_b(x)$, $K(x)$, and $M_h(x)$ as constants, and their terminus values. Unless otherwise stated, going forwards we will take these variables to refer to their values at the terminus. However, since $\sigma - \sigma_0(x)$ is small and changes sign within the boundary layer (Figure 3a), we retain the next term in its expansion, which is linear in x . Under these approximations, (Equation B13) becomes

$$\frac{\partial^2 \hat{b}}{\partial x^2} = \frac{\rho_i K \kappa^2}{Q_b M_h} \left(\sigma(\kappa) - \sigma_0(x_t) + \frac{\partial \sigma_0}{\partial x} (x_t - x) \right) \hat{b}. \quad (\text{B14})$$

Recognizing this differential equation structure as Airy's equation, we see that in the limit of small wavelengths, the structure of the gap height perturbation $\hat{b}(x)$ must be a rescaled Airy function. By scaling the growth rate $\sigma - \sigma_0(x_i)$ and the inland distance x using

$$\sigma_0(x_i) - \sigma = \Sigma \left(\frac{\partial \sigma_0}{\partial x} \right)^{2/3} \left(\frac{Q_b M_h}{\rho_i K \kappa^2} \right)^{1/3}, \quad x_i - x = \left(\frac{Q_b M_h}{\rho_i K \kappa^2 (\partial \sigma_0 / \partial x)} \right)^{1/3} X, \quad (\text{B15})$$

Equation B14 simplifies to

$$\frac{\partial^2 \hat{b}}{\partial X^2} = (X - \Sigma) \hat{b}, \quad (\text{B16})$$

exactly Airy's equation with a shifted coordinate system, with the rescaled growth rate Σ setting the shift. Since we require our perturbations decay inland, \hat{b} must be an Airy function of the first kind, that is, $\hat{b} = \text{Ai}(X - \Sigma)$, and substituting this into Equation B12,

$$\hat{h} = \left(\frac{Q_b}{K \kappa^2} \right)^{2/3} \left(\frac{\rho_i (\partial \sigma_0 / \partial x)}{M_h} \right)^{1/3} \text{Ai}'(X - \Sigma). \quad (\text{B17})$$

Thus, to match on to atmospheric pressure, Σ is chosen so that $\hat{h}(0) = \text{Ai}'(-\Sigma) = 0$, so $\Sigma = 1.0187\dots$ and

$$\sigma = \sigma_0(x_i) - \Sigma \left(\frac{\partial \sigma_0}{\partial x} \right)^{2/3} \left(\frac{Q_b M_h}{\rho_i K \kappa^2} \right)^{1/3}. \quad (\text{B18})$$

While there are infinitely many other possible values of z such that $\text{Ai}'(-z) = 0$, they are increasingly large, and so associated with smaller growth rates; the associated perturbations are always more stable and less relevant to the dynamics of the system.

B2. Inclusion of Lateral Heat Transport

As before, since the gap height is small, we expect strong gradients in z , and since we wish to capture the short-wavelength behavior, we also retain gradients in y . In this limit, the linearized form of the heat Equation 25 reduces to diffusion of temperature with a heat source,

$$-k \left(\frac{\partial^2 \hat{T}}{\partial z^2} - \kappa^2 \hat{T} \right) = \hat{Q}. \quad (\text{B19})$$

The boundary conditions remain a geothermal flux at the base, and that the ice-water interface is at melting temperature, which in terms of the perturbed quantities become

$$-k \frac{\partial \hat{T}}{\partial z} \Big|_{z=0} = 0, \quad \frac{\partial \hat{T}}{\partial z} \Big|_{z=\bar{b}} \hat{b} + \hat{T}(\bar{b}) = \hat{T}(\bar{b}) - \frac{\bar{m}L}{k} \hat{b} = 0. \quad (\text{B20})$$

We solve the linearized diffusion Equation B19 with these boundary conditions, and find that the profile of the corresponding temperature change is

$$\hat{T} = \left[\left(\frac{\bar{m}L}{k} \hat{b} - \frac{\hat{Q}}{k \kappa^2} \right) \frac{\cosh(\kappa z)}{\cosh(\kappa \bar{b})} + \frac{\hat{Q}}{k \kappa^2} \right], \quad (\text{B21})$$

and in particular the additional heat flux into the ice is

$$-k \frac{\partial \hat{T}}{\partial z} \Big|_{z=\bar{b}} - k \frac{\partial^2 \hat{T}}{\partial z^2} \Big|_{z=\bar{b}} \hat{b} = \frac{\tanh(\kappa \bar{b})}{\kappa} \hat{Q} + (\bar{Q} - \kappa \tanh(\kappa \bar{b}) \bar{m}L) \hat{b}, \quad (\text{B22})$$

which, equating to the latent heat of melting $\hat{m}L$, corresponds to a melt-rate perturbation

$$\hat{m} = \frac{1}{L} \left(\frac{\tanh(\kappa \bar{b})}{\kappa} \hat{Q} + (\bar{Q} - \kappa \tanh(\kappa \bar{b}) \bar{m}L) \hat{b} \right). \quad (\text{B23})$$

To simplify this further, we consider the case where the background gap height is small, so $\tanh(\kappa \bar{b}) \approx \kappa \bar{b}$. Then (Equation B23) becomes

$$\hat{m} = \frac{1}{L} (\hat{Q} \bar{b} + \bar{Q} \hat{b}) - \kappa^2 \bar{b} \bar{m} \hat{b} = \hat{m}_0 - \kappa^2 \bar{b} \bar{m} \hat{b}, \quad (\text{B24})$$

where \hat{m}_0 is the perturbation in melt-rate when ignoring lateral heat transport, previously found in Equation B8. We see that including lateral diffusion of heat has introduced a new term proportional to $-\kappa^2 \hat{b}$, which has the structure of a diffusion of gap height away from narrowly channelizing regions. Equation B24 is structurally similar to Equation 14 of Walder (1982), although the rest of that analysis proceeded to neglect the diffusion term, arguing it was too small to impact the water layer dynamics, which is true except when κ becomes very large.

We now demonstrate that our lateral heat diffusion term regularizes the linear stability analysis. With the new melt-diffusion term modifying the melt-rate perturbation from Equation B8 into Equation B24, Equations B9 and B11 for the structure of the pressure head \hat{h} and gap height \hat{b} perturbations are slightly modified to

$$\left(\sigma - \frac{M_b}{\rho_i} + A \bar{N}^n + \frac{u_b}{l_r} + \frac{\bar{m} \bar{b}}{\rho_i} \kappa^2 \right) \hat{b} = \left(A n \bar{N}^{n-1} \rho_w g \bar{b} - \frac{U}{\rho_i} \right) \hat{h} - \frac{M_h}{\rho_i} \frac{\partial \hat{h}}{\partial x} + \frac{\partial}{\partial x} \left(\frac{\bar{m} \bar{b}}{\rho_i} \frac{\partial \hat{b}}{\partial x} \right), \quad (\text{B25})$$

and

$$\sigma \hat{b} = -\frac{\partial}{\partial x} \left(Q_b \hat{b} - Q_h \frac{\partial \hat{h}}{\partial x} \right) - K \kappa^2 \hat{h} + \frac{M_b}{\rho_w} \hat{b} - \frac{U}{\rho_w} \hat{h} - \frac{M_h}{\rho_w} \frac{\partial \hat{h}}{\partial x} - \frac{\bar{m} \bar{b}}{\rho_w} \kappa^2 \hat{b} + \frac{\partial}{\partial x} \left(\frac{\bar{m} \bar{b}}{\rho_w} \frac{\partial \hat{b}}{\partial x} \right). \quad (\text{B26})$$

This is once again an eigenvalue problem to find the growth rate σ corresponding to \hat{h} and \hat{b} which can only be solved numerically in general (Figure 5).

However, if we anticipate only a small change from our previous analysis, we can go through the same simplifications and once again look primarily at the large κ (small wavelength) case, taking the same limit of small pressure variations, $\hat{h} \ll 1$, and channels confined close to the terminus, $1/\kappa \ll x \ll 1$. Under these assumptions, Equations B25 and B26 reduce to

$$\left(\sigma - \frac{M_b}{\rho_i} + A \bar{N}^n + \frac{u_b}{l_r} + \frac{\bar{m} \bar{b}}{\rho_i} \kappa^2 \right) \hat{b} = -\frac{M_h}{\rho_i} \frac{\partial \hat{h}}{\partial x}, \quad (\text{B27})$$

and

$$K \kappa^2 \hat{h} = -Q_b \frac{\partial \hat{b}}{\partial x}. \quad (\text{B28})$$

These are structurally identical to the previous large κ limit, but with an additional $\bar{m} \bar{b} \kappa^2 / \rho_i$ multiplying \hat{b} in Equation B27. This means σ_D , the growth rate when $\hat{h} = 0$, is now

$$\sigma_D = \frac{M_b}{\rho_i} - A\bar{N}^n - \frac{u_b}{l_r} - \frac{\bar{m}\bar{b}}{\rho_i}\kappa^2 = \sigma_0(x_i) - \frac{\bar{m}\bar{b}}{\rho_i}\kappa^2 \quad (\text{B29})$$

and becomes stable as κ gets large.

B3. The Case of Cold Ice

Throughout this paper, we have assumed the ice to be at melting point, neglecting heat fluxes into the ice. However, if there is a temperature gradient through the ice, tending toward a cold surface temperature, we should modify the balance of heat fluxes at the melting interface to include this loss toward the surface,

$$\dot{m}L = -k_w \frac{\partial T_w}{\partial n} + k_i \frac{\partial T_i}{\partial n}, \quad (\text{B30})$$

where k_w is the thermal conductivity of water and k_i is that of ice.

The analysis of heat fluxes in the water layer proceeds exactly as in Section 3.3. In the ice, $T_i = \bar{T}_i + \hat{T}_i e^{iky}$ solves the heat equation with no heat source term, and, given the flow speed of ice, no advection term, so

$$\frac{d^2 \hat{T}_i}{dz^2} - \kappa^2 \hat{T}_i = 0. \quad (\text{B31})$$

Assuming that the ice is much deeper than the wavelength of the perturbations, temperature fluctuations decay toward the surface. Thus, the solution to Equation B31 with $T_i(b) = T_m$ is given by

$$\hat{T}_i = -\frac{d\bar{T}_i}{dz} \hat{b} e^{-\kappa(z-\bar{b})} \quad (\text{B32})$$

and the perturbed heat flux into the ice is

$$k_i \frac{\partial \hat{T}_i}{\partial z} = k_i \frac{d\bar{T}_i}{dz} \kappa \hat{b}. \quad (\text{B33})$$

Inserting Equation B33 into Equation B30 we obtain, in the notation of Equation B24

$$\hat{m} = \hat{m}_0 - \kappa^2 \bar{b} \bar{m} \hat{b} + \frac{k_i}{L} \frac{d\bar{T}_i}{dz} \kappa \hat{b}. \quad (\text{B34})$$

Note that the temperature gradient through the ice is negative, so this additional term also stabilizes the short wavelengths, representing the stabilizing effects of lateral heat flux through the ice as well as through the water.

Thus, the analytic expression for the growth rate of perturbations in the case of cold ice is, by comparison with Equation 45,

$$\sigma = \sigma_0(x_i) - \frac{\bar{m}\bar{b}}{\rho_i}\kappa^2 - \frac{k_i}{\rho_i L} \left| \frac{d\bar{T}_i}{dz} \right| \kappa - \Sigma \left(\frac{\partial \sigma_0}{\partial x} \right)^{2/3} \left(\frac{Q_b M_h}{\rho_i K \kappa^2} \right)^{1/3}. \quad (\text{B35})$$

Note that the background state also changes due to the reduction in melt-rate, since heat is lost into the ice, so

$$\bar{m} = \frac{1}{L} \left(G - k_i \left| \frac{d\bar{T}_i}{dz} \right| + |\mathbf{u}_b \cdot \boldsymbol{\tau}_b| - \rho_w g \bar{q} \frac{d\bar{h}}{dx} \right). \quad (\text{B36})$$

Structurally this acts like a reduction in G and can be incorporated into the stability criterion in this way.

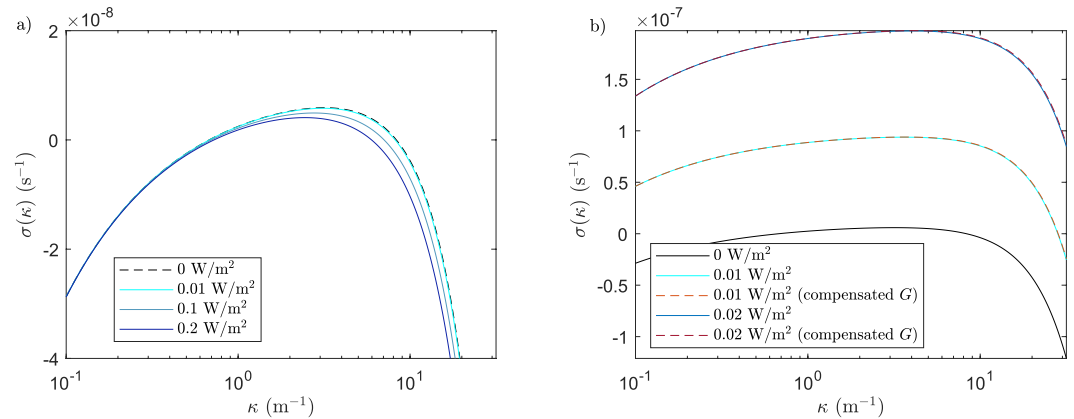


Figure B1. Impact of including a heat flux into the ice on the growth rate of perturbations, as given by Equation B35. (a) Increasing G to compensate, so that the background state remains the same. This isolates the stabilizing impact of lateral heat flux within the ice, which is minimal for realistic temperature gradients. (b) Keeping G fixed, and thus with a lower net background heat flux. Dashed lines show equivalent curves for appropriately reduced G and temperate ice, indicating that altering G accounts for the majority of the change in dynamics.

Plots of the growth rate Equation B35 for a range of temperature gradients are shown in Figure B1. Figure B1a shows that if the net background heat flux, $G - k_i |dT_i/dz|$, is unchanged, then the stabilizing impact of lateral heat flux through the ice has minimal impact on the growth rates of perturbations for realistic values of the ice temperature gradient. However, Figure B1b shows that if G is kept fixed, the reduction in net background heat flux affects the growth rate much more dramatically, simply because decreasing the net background heat flux reduces the value of \bar{b} , which increases σ_0 . For comparison, just changing the value of G without including heat fluxes through the ice yields extremely similar results.

We therefore suggest that vertical temperature gradients within the ice should be accounted for via a reduction in G , but lateral temperature gradients have very little impact on the evolution of the subglacial hydrology and can be ignored in modeling.

B4. Strongly Varying Ice Thickness

Our analysis has assumed that the maximum value of $\sigma_0(x)$ is always found at the terminus. This is true in our numerical examples, when the effective pressure tends to increase toward the terminus. However, if there is a very strong gradient in ice overburden pressure, the maximum growth rate can occur slightly inland. We jump to the large κ limit to see how this modifies the analytical growth rates.

In this case, perturbations are expected to occur localized around this maximum at $x = x_{\max}$, rather than around the terminus. The relevant leading order expansion for $\sigma - \sigma_0(x)$ is now a quadratic,

$$\sigma_0(x) \approx \sigma_0(x_{\max}) + \frac{1}{2} \frac{d^2 \sigma_0}{dx^2} (x - x_{\max})^2, \quad (\text{B37})$$

and we approximate all other functions of x by their values at x_{\max} (rather than their values at the terminus).

Substituting this altered shape of the growth rate, the perturbed kinematic condition is

$$\left(\sigma - \sigma_0(x_{\max}) - \frac{1}{2} \frac{d^2 \sigma_0}{dx^2} (x - x_{\max})^2 \right) \hat{b} = -\frac{M_h}{\rho_i} \frac{\partial \hat{h}}{\partial x} \quad (\text{B38})$$

while the perturbed conservation of mass is unchanged except in where Q_b and K are evaluated,

$$Q_b \frac{\partial \hat{b}}{\partial x} = -K \kappa^2 \hat{h}. \quad (\text{B39})$$

Combining these, we have

$$\frac{\partial^2 \hat{b}}{\partial x^2} = -\frac{K\kappa^2}{Q_b} \frac{\partial \hat{h}}{\partial x} = \frac{\rho_i K \kappa^2}{Q_b M_h} \left(\sigma - \sigma_0(x_{\max}) - \frac{1}{2} \frac{d^2 \sigma_0}{dx^2} (x - x_{\max})^2 \right) \hat{b}. \quad (\text{B40})$$

To make progress, we now rescale with

$$\sigma(\kappa) - \sigma_0(x_{\max}) = a \sqrt{\frac{2 \left| \frac{d^2 \sigma_0}{dx^2} \right| Q_b M_h}{\rho_i K \kappa^2}}, \quad z = \left(\frac{2 \left| \frac{d^2 \sigma_0}{dx^2} \right| \rho_i K \kappa^2}{Q_b M_h} \right)^{1/4} (x - x_{\max}) \quad (\text{B41})$$

and obtain

$$\frac{\partial^2 \hat{b}}{\partial z^2} = \left(a + \frac{z^2}{4} \right) \hat{b}. \quad (\text{B42})$$

We look for values of a that permit a solution that decays as $z \rightarrow \pm\infty$, so as to fit both the upstream boundary condition (decay of the perturbation toward the ice divide, $z \rightarrow -\infty$) and downstream (imposed pressure head at the margin requiring decay as $z \rightarrow \infty$).

A symmetrically decaying solution to Equation B42 is possible whenever

$$\sin\left(\left(\frac{a}{2} + \frac{1}{4}\right)\pi\right) \Gamma\left(\frac{3}{4} - \frac{a}{2}\right) = 0, \quad (\text{B43})$$

but we want the maximum possible value of a , associated with the largest growth rate. This turns out to be $a = -1/2$, so

$$\sigma(\kappa) = \sigma_0(x_{\max}) - \sqrt{\frac{\left| \frac{d^2 \sigma_0}{dx^2} \right| Q_b M_h}{2\rho_i K \kappa^2}}, \quad (\text{B44})$$

and the growth rate at large wavelengths now decays like $1/\kappa$. The associated shape of the gap height perturbation

$$\hat{b} = \exp\left(-\left(\frac{2 \left| \frac{d^2 \sigma_0}{dx^2} \right| \rho_i K \kappa^2}{Q_b M_h}\right)^{1/2} \frac{(x - x_{\max})^2}{4}\right) \quad (\text{B45})$$

is Gaussian function peaked around $x = x_{\max}$

Data Availability Statement

Code for calculating the laterally uniform profiles, eigenfunctions, and growth rates, is available on Zenodo (Warburton, 2024). Basilisk (Popinet, 2013–2024) now includes the Basilisk implementation of SHAKTI. Simulations with the original implementation of SHAKTI (Sommers et al., 2018) were done in ISSM Version 4.21 (Larour et al., 2012). MEaSURES velocity data (Joughin et al., 2018) is available from Joughin et al. (2016). We used BedMachine Version 4 (Morlighem et al., 2017).

Acknowledgments

KLPW was funded by the Dartmouth Society of Fellows; CRM acknowledges funding from NSF (2012958), NASA (EPSCoR-80NSSC21M0329), the Army Research Office (7881IEG), and the Heising-Simons Foundation (2020–1911); and ANS was supported by the Heising-Simons Foundation (2020–1911). We thank Mathieu Morlighem for support in sharing the domain outline containing Russell Glacier and Isunnguata Sermia, and Lauren Andrews for helpful discussion. Our thanks to the editor and three anonymous reviewers for their time and helpful suggestions in improving this manuscript.

References

Andrews, L. C., Catania, G. A., Hoffman, M. J., Gullep, J. D., Lüthi, M. P., Ryser, C., et al. (2014). Direct observations of evolving subglacial drainage beneath the Greenland Ice Sheet. *Nature*, *514*(7520), 80–83. <https://doi.org/10.1038/nature13796>

Aschwanden, A., Fahnestock, M. A., Truffer, M., Brinkerhoff, D. J., Hock, R., Khroulev, C., et al. (2019). Contribution of the Greenland Ice Sheet to sea level over the next millennium. *Science Advances*, *5*(6), eaav9396. <https://doi.org/10.1126/sciadv.aav9396>

Bartholomew, I., Nienow, P., Sole, A., Mair, D., Cowton, T., Palmer, S., & Wadhwa, J. (2011). Supraglacial forcing of subglacial drainage in the ablation zone of the Greenland ice sheet. *Geophysical Research Letters*, *38*(8). <https://doi.org/10.1029/2011GL047063>

Benn, D. I., Fowler, A. C., Hewitt, I., & Sevestre, H. (2019). A general theory of glacier surges. *Journal of Glaciology*, *65*(253), 701–716. <https://doi.org/10.1017/jog.2019.62>

Brinkerhoff, D. J., Aschwanden, A., & Fahnestock, M. (2021). Constraining subglacial processes from surface velocity observations using surrogate-based bayesian inference. *Journal of Glaciology*, *67*(263), 385–403. <https://doi.org/10.1017/jog.2020.112>

Brinkerhoff, D. J., Meyer, C. R., Bueler, E., Truffer, M., & Bartholomew, T. C. (2016). Inversion of a glacier hydrology model. *Annals of Glaciology*, *57*(72), 84–95. <https://doi.org/10.1017/aog.2016.3>

Cornford, S. L., Martin, D. F., Lee, V., Payne, A. J., & Ng, E. G. (2016). Adaptive mesh refinement versus subgrid friction interpolation in simulations of Antarctic ice dynamics. *Annals of Glaciology*, *57*(73), 1–9. <https://doi.org/10.1017/aog.2016.13>

de Fleurian, B., Werder, M. A., Beyr, S., Brinkerhoff, D. J., Delaney, I., Dow, C. F., et al. (2018). SHMIP the subglacial hydrology model intercomparison Project. *Journal of Glaciology*, *64*(248), 897–916. <https://doi.org/10.1017/jog.2018.78>

Dow, C. F. (2022). The role of subglacial hydrology in antarctic ice sheet dynamics and stability: A modelling perspective. *Annals of Glaciology*, *63*(87–89), 49–54. <https://doi.org/10.1017/aog.2023.9>

Felden, A. M., Martin, D. F., & Ng, E. G. (2023). SUHMO: An adaptive mesh refinement subglacial hydrology model v1.0. *Geoscientific Model Development*, *16*(1), 407–425. <https://doi.org/10.5194/gmd-16-407-2023>

Flowers, G. E. (2015). Modelling water flow under glaciers and ice sheets. *Proceedings of the Royal Society A: Mathematical, Physical and Engineering Sciences*, *471*(2176), 20140907. <https://doi.org/10.1098/rspa.2014.0907>

Hager, A. O., Hoffman, M. J., Price, S. F., & Schroeder, D. M. (2022). Persistent, extensive channelized drainage modeled beneath Thwaites Glacier, West Antarctica. *The Cryosphere*, *16*(9), 3575–3599. <https://doi.org/10.5194/tc-16-3575-2022>

Helanow, C., Iverson, N. R., Woodard, J. B., & Zoet, L. K. (2021). A slip law for hard-bedded glaciers derived from observed bed topography. *Science Advances*, *7*(20), eabe7798. <https://doi.org/10.1126/sciadv.abe7798>

Hewitt, D. R., Chini, G. P., & Neufeld, J. A. (2018). The influence of a poroelastic till on rapid subglacial flooding and cavity formation. *Journal of Fluid Mechanics*, *855*, 1170–1207. <https://doi.org/10.1017/jfm.2018.624>

Hewitt, I. J. (2009). *Mathematical modelling of geophysical melt drainage (PhD thesis)*. University of Oxford.

Hewitt, I. J. (2011). Modelling distributed and channelized subglacial drainage: The spacing of channels. *Journal of Glaciology*, *57*(202), 302–314. <https://doi.org/10.3189/002214311796405951>

Hewitt, I. J. (2013). Seasonal changes in ice sheet motion due to melt water lubrication. *Earth and Planetary Science Letters*, *371*–372, 16–25. <https://doi.org/10.1016/j.epsl.2013.04.022>

Hiestler, J., Sergienko, O. V., & Hulbe, C. L. (2016). Topographically mediated ice stream subglacial drainage networks. *Journal of Geophysical Research: Earth Surface*, *121*(2), 497–510. <https://doi.org/10.1002/2015JF003660>

Hill, T., Flowers, G. E., Hoffman, M. J., Bingham, D., & Werder, M. A. (2023). Improved representation of laminar and turbulent sheet flow in subglacial drainage models. *Journal of Glaciology*, 1–14. <https://doi.org/10.1017/jog.2023.103>

Joughin, I., Smith, B., Howat, I., & Scambos, T. (2016). Measures multi-year Greenland ice sheet velocity mosaic (nsidc-0670, version 1) [Dataset]. <https://doi.org/10.5067/QUA5Q9SVMSJG>

Joughin, I., Smith, B. E., & Howat, I. M. (2018). A complete map of Greenland ice velocity derived from satellite data collected over 20 years. *Journal of Glaciology*, *64*(243), 1–11. <https://doi.org/10.1017/jog.2017.73>

Kyrke-Smith, T. M., Katz, R. F., & Fowler, A. C. (2014). Subglacial hydrology and the formation of ice streams. *Proceedings of the Royal Society A: Mathematical, Physical and Engineering Sciences*, *470*(2161), 20130494. <https://doi.org/10.1098/rspa.2013.0494>

Larour, E., Seroussi, H., Morlighem, M., & Rignot, E. (2012). Continental scale, high order, high spatial resolution, ice sheet modeling using the ice sheet system model (issm). *Journal of Geophysical Research*, *117*(F1). <https://doi.org/10.1029/2011JF002140>

MacGregor, J. A., Fahnestock, M. A., Catania, G. A., Aschwanden, A., Clow, G. D., Colgan, W. T., et al. (2016). A synthesis of the basal thermal state of the Greenland Ice Sheet. *Journal of Geophysical Research: Earth Surface*, *121*(7), 1328–1350. <https://doi.org/10.1002/2015JF003803>

Maier, N., Humphrey, N., Harper, J., & Meierbachtol, T. (2019). Sliding dominates slow-flowing margin regions, Greenland Ice Sheet. *Science Advances*, *5*(7), eaaw5406. <https://doi.org/10.1126/sciadv.aaw5406>

Moon, T., Joughin, I., Smith, B., van den Broeke, M. R., van de Berg, W. J., Noël, B., & Usher, M. (2014). Distinct patterns of seasonal Greenland glacier velocity. *Geophysical Research Letters*, *41*(20), 7209–7216. <https://doi.org/10.1002/2014GL061836>

Morlighem, M., Rignot, E., Seroussi, H., Larour, E., Ben Dhia, H., & Aubry, D. (2010). Spatial patterns of basal drag inferred using control methods from a full-Stokes and simpler models for pine island glacier, west Antarctica. *Geophysical Research Letters*, *37*(14). <https://doi.org/10.1029/2010GL043853>

Morlighem, M., Williams, C. N., Rignot, E., An, L., Arndt, J. E., Bamber, J. L., et al. (2017). Bedmachine v3: Complete bed topography and ocean bathymetry mapping of Greenland from multibeam echo sounding combined with mass conservation. *Geophysical Research Letters*, *44*(21), 11051–11061. <https://doi.org/10.1002/2017GL074954>

Mouginot, J., Rignot, E., Björk, A. A., Van den Broeke, M., Millan, R., Morlighem, M., et al. (2019). Forty-six years of Greenland Ice Sheet mass balance from 1972 to 2018. *Proceedings of the National Academy of Sciences*, *116*(19), 9239–9244. <https://doi.org/10.1073/pnas.1904242116>

Nienow, P. W., Sole, A. J., Slater, D. A., & Cowton, T. R. (2017). Recent advances in our understanding of the role of meltwater in the Greenland ice sheet system. *Current Climate Change Reports*, *3*(4), 330–344. <https://doi.org/10.1007/s40641-017-0083-9>

Otosaka, I., Shepherd, A., Ivins, E., Schlegel, N., Amory, C., van den Broeke, M., et al. (2023). Mass balance of the Greenland and Antarctic ice sheets from 1992 to 2020. *Earth System Science Data*, *15*(4), 1597–1616. <https://doi.org/10.5194/essd-15-1597-2023>

Poinar, K. (2023). Seasonal flow types of glaciers in Sermilik fjord, Greenland, over 2016–2021. *Journal of Geophysical Research: Earth Surface*, *128*(7), e2022JF006901. <https://doi.org/10.1029/2022JF006901>

Poinar, K., Dow, C. F., & Andrews, L. C. (2019). Long-term support of an active subglacial hydrologic system in Southeast Greenland by firm aquifers. *Geophysical Research Letters*, *46*(9), 4772–4781. <https://doi.org/10.1029/2019GL028276>

Popinet, S. (2013–2024). Basilisk [Software]. <http://basilisk.fr>

Rada, C., & Schoof, C. (2018). Channelized, distributed, and disconnected: Subglacial drainage under a valley glacier in the Yukon. *The Cryosphere*, *12*(8), 2609–2636. <https://doi.org/10.5194/tc-12-2609-2018>

- Rignot, E., & Mouginot, J. (2012). Ice flow in Greenland for the international polar year 2008–2009. *Geophysical Research Letters*, 39(11). <https://doi.org/10.1029/2012GL051634>
- Schoof, C. (2005). The effect of cavitation on glacier sliding. *Proceedings of the Royal Society A: Mathematical, Physical and Engineering Sciences*, 461(2055), 609–627. <https://doi.org/10.1098/rspa.2004.1350>
- Schoof, C. (2010). Ice-sheet acceleration driven by melt supply variability. *Nature*, 468(7325), 803–806. <https://doi.org/10.1038/nature09618>
- Schoof, C. (2023). The evolution of isolated cavities and hydraulic connection at the glacier bed. Part 1: Steady states and friction laws. *EGU Sphere*, 2023, 1–27. <https://doi.org/10.5194/egusphere-2022-1380>
- Schoof, C., Hewitt, I. J., & Werder, M. A. (2012). Flotation and free surface flow in a model for subglacial drainage. part 1. distributed drainage. *Journal of Fluid Mechanics*, 702, 126–156. <https://doi.org/10.1017/jfm.2012.165>
- Seroussi, H., Morlighem, M., Rignot, E., Khazendar, A., Larour, E., & Mouginot, J. (2013). Dependence of century-scale projections of the Greenland ice sheet on its thermal regime. *Journal of Glaciology*, 59(218), 1024–1034. <https://doi.org/10.3189/2013JoG13J054>
- Shapiro, D. R., Joughin, I. R., Poinar, K., Morlighem, M., & Gillet-Chaulet, F. (2016). Basal resistance for three of the largest Greenland outlet glaciers. *Journal of Geophysical Research: Earth Surface*, 121(1), 168–180. <https://doi.org/10.1002/2015JF003643>
- Sommers, A., Meyer, C., Morlighem, M., Rajaram, H., Poinar, K., Chu, W., & Mejia, J. (2023). Subglacial hydrology modeling predicts high winter water pressure and spatially variable transmissivity at Helheim Glacier, Greenland. *Journal of Glaciology*, 1–13. <https://doi.org/10.1017/jog.2023.39>
- Sommers, A., Rajaram, H., & Morlighem, M. (2018). SHAKTI: Subglacial hydrology and kinetic, transient interactions v1.0. *Geoscientific Model Development*, 11(7), 2955–2974. <https://doi.org/10.5194/gmd-11-2955-2018>
- Tedstone, A. J., Nienow, P. W., Gourmelen, N., Dehecq, A., Goldberg, D., & Hanna, E. (2015). Decadal slowdown of a land-terminating sector of the Greenland ice sheet despite warming. *Nature*, 526(7575), 692–695. <https://doi.org/10.1038/nature15722>
- Vijay, S., King, M. D., Howat, I. M., Solgaard, A. M., Khan, S. A., & Noël, B. (2021). Greenland ice-sheet wide glacier classification based on two distinct seasonal ice velocity behaviors. *Journal of Glaciology*, 67(266), 1241–1248. <https://doi.org/10.1017/jog.2021.89>
- Walder, J. S. (1982). Stability of sheet flow of water beneath temperate glaciers and implications for glacier surging. *Journal of Glaciology*, 28(99), 273–293. <https://doi.org/10.1017/s0022143000011631>
- Warburton, K. L. P. (2024). kasiawarburton/shaktistability [Software]. <https://doi.org/10.5281/zenodo.10887090>
- Warburton, K. L. P., Hewitt, D. R., & Neufeld, J. A. (2023). Shear dilation of subglacial till results in time-dependent sliding laws. *Proceedings of the Royal Society A: Mathematical, Physical and Engineering Sciences*, 479(2269), 20220536. <https://doi.org/10.1098/rspa.2022.0536>
- Werder, M. A., Hewitt, I. J., Schoof, C. G., & Flowers, G. E. (2013). Modeling channelized and distributed subglacial drainage in two dimensions. *Journal of Geophysical Research: Earth Surface*, 118(4), 2140–2158. <https://doi.org/10.1002/jgrf.20146>
- Zimmerman, R. W., Al-Yaarubi, A., Pain, C. C., & Grattoni, C. A. (2004). Non-linear regimes of fluid flow in rock fractures. *International Journal of Rock Mechanics and Mining Sciences*, 41, 163–169. <https://doi.org/10.1016/j.ijrmms.2004.03.036>
- Zoet, L. K., & Iverson, N. R. (2020). A slip law for glaciers on deformable beds. *Science*, 368(6486), 76–78. <https://doi.org/10.1126/science.aaz1183>
- Zwally, H. J., Abdalati, W., Herring, T., Larson, K., Saba, J., & Steffen, K. (2002). Surface melt-induced acceleration of Greenland ice-sheet flow. *Science*, 297(5579), 218–222. <https://doi.org/10.1126/science.1072708>